Feasibility and Mass-Benefit Analysis of Aerocapture for Missions to Venus

Athul Pradeepkumar Girija,* Ye Lu,† and Sarag J. Saikia‡
Purdue University, West Lafayette, Indiana 47907

https://doi.org/10.2514/1.A34529

A numerical assessment of the feasibility of aerocapture at Venus is presented, and the mass benefit of aerocapture is compared with propulsive orbit insertion. This paper considers constraints imposed by entry corridor, deceleration loads, and aerodynamic heating on aerocapture for two vehicle control techniques: lift modulation and drag modulation. Feasibility charts are presented to graphically visualize the aerocapture design space spanning interplanetary trajectory and vehicle performance. Results indicate lift modulation aerocapture is feasible at Venus using existing blunt-body aeroshells. Drag modulation technique is also feasible and an attractive option for small satellites, but merits an additional study due to small corridor width and heating constraints. The peak heat rate is within the capability of existing thermal protection system materials for both control techniques. Delivered mass fraction using aerocapture is compared with propulsive insertion with and without aerobraking. Aerocapture allows 90–250% increase in delivered mass to a 400 km circular orbit compared with propulsive insertion.

Nomenclature

A	=	aerodynamic reference area, m^2
C_D	=	coefficient of drag
C_L	=	coefficient of lift
C_3	=	characteristic energy, km^2/s^2
D	=	aerodynamic drag force, N
f_{ESS}	=	entry-support-system mass fraction
f_P	=	overall payload mass fraction for mission architecture
$f_{P,\text{entry}}$	=	entry-system useful payload mass fraction
$f_{P,\text{Venus entry}}$	=	entry useful payload mass fraction for Venus entry
f_{TPS}	=	thermal protection system mass fraction
$f_{\text{TPS,Venus entry}}$	=	thermal protection system mass fraction for Venus entry
G	=	peak deceleration load, Earth g
g, g_0	=	standard acceleration due to gravity on the surface of Earth, m/s^2
g_r	=	radial component of gravitational acceleration, m/s^2
g_θ	=	longitudinal component of gravitational acceleration, m/s^2
g_ϕ	=	latitudinal component of gravitational acceleration, m/s^2
I_{sp}	=	propulsion system specific impulse, s
J_2, J_3, J_4	=	zonal harmonic terms
K	=	constant in Sutton–Graves empirical relation
K_1, K_2, K_3	=	constants in radiative heating correlation
L	=	aerodynamic lift force, N
L/D	=	lift-to-drag ratio
$(L/D)_{\text{trim}}$	=	hypersonic trim lift-to-drag ratio
m	=	vehicle mass, kg
Q	=	integrated heat load, J/cm^2
q	=	dynamic pressure, N/m^2
$\dot{q}$	=	total stagnation-point heat rate, W/cm^2
$\dot{q}_c$	=	stagnation-point convective heat rate, W/cm^2
$\dot{q}_r$	=	stagnation-point radiative heat rate, W/cm^2
r	=	radial distance from the center of the planet, m
r_p	=	mean equatorial radius of the planet, m
r_{pe}	=	periapsis radius of the capture orbit, m
U	=	gravitational potential
V	=	planet-relative velocity, m/s
V_e	=	planet-relative entry velocity at atmospheric entry interface, m/s
$V_{e,i}$	=	inertial entry velocity at atmospheric entry interface, m/s
V_{pe}	=	orbital speed of the capture orbit at periapsis, m/s
V_∞	=	hyperbolic excess speed, m/s
β	=	ballistic coefficient, kg/m^2
β_1	=	ballistic coefficient before drag skirt separation, kg/m^2
β_2	=	ballistic coefficient after drag skirt separation, kg/m^2
β_2/β_1	=	ballistic coefficient ratio
γ	=	planet-relative flight-path angle; angle between the local horizontal plane and the velocity vector, rad
ΔV	=	velocity increment or decrement, m/s
ϵ	=	additional margin over the required corridor width, deg
θ	=	longitude, rad
μ_p	=	standard gravitational parameter of the planet, m^3/s^2
ρ	=	atmospheric density, kg/m^3
ρ_∞	=	freestream atmospheric density, kg/m^3
σ	=	bank angle, rad
ϕ	=	latitude, rad
Ω	=	planet rotation rate, rad/s
ψ	=	planet-relative heading angle, rad

Subscripts

ac	=	aerocapture insertion
e	=	value at atmospheric entry interface
max	=	maximum value
min	=	minimum value
prop	=	propulsive insertion

Received 15 April 2019; revision received 2 August 2019; accepted for publication 25 November 2019; published online 27 December 2019.

*Doctoral Candidate, School of Aeronautics and Astronautics; apradee@purdue.edu. Student Member AIAA.

†Doctoral Candidate, School of Aeronautics and Astronautics; yelu@purdue.edu. Student Member AIAA.

‡Research Assistant Professor, School of Aeronautics and Astronautics; ssaikia@purdue.edu.

I. Introduction

AEROCAPTURE is a maneuver, in which a spacecraft uses aerodynamic force from a single pass through a planetary atmosphere to decelerate and achieve orbit insertion (OI). Aerocapture is a promising alternative to propulsive OI at atmosphere-bearing destinations in the solar system, as it can save propellant mass and enable some missions beyond the propulsive ΔV capability [1]. Aerocapture can allow a lighter spacecraft and enable OI from interplanetary trajectories traditionally not feasible using propulsive insertion. Aerocapture has been proposed for several mission concepts and technology demonstration flights, but has never been flown [2–5]. Hall et al. [1] showed aerocapture could enhance missions to Venus, Mars, Titan, and Uranus, and enable some missions to Jupiter, Saturn, and Neptune. Existing aeroshell technologies and thermal protection system (TPS) materials are feasible for aerocapture missions to Venus, Mars, and Titan. Missions to Uranus and Neptune using aerocapture may require the development of mid-L/D aeroshells. Aerocapture on Jupiter and Saturn is a long-term goal, as their huge gravity wells result in very high entry speeds and harsh aerothermal environments beyond the capability of existing TPS materials [6].

Aerocapture has been investigated as a potential planetary capture mode since the 1960s, and some authors have referred to it as aerobraking [7,8]. One of the earliest papers describing the aerocapture mission concept can be attributed to Cruz [9] in 1979, which focused on an aerocapture system for a Mars sample return mission. Until the late 1990s, most of the aerocapture literature focuses on robotic and human missions to Mars. Detailed analysis of aerocapture on Venus that began only in the early 2000s primarily attributed to a multicenter NASA effort as part of the In-Space Technology Program aerocapture studies [10]. The study assessed the benefits offered by Venus aerocapture, identified the associated risks, and proposed technology developments to mitigate such risks. The study concluded that Venus aerocapture is feasible and required no new enabling technologies.

Craig and Lyne [11] performed a parametric study of Venus aerocapture using two vehicle lift-to-drag (L/D) ratios and a range of entry velocities. The study evaluated the corridor width (the range of entry flight-path angles acceptable to perform aerocapture), deceleration loads, heat rate, and heat loads for an Apollo-type vehicle performing aerocapture on Venus. Hall et al. [1] conducted a cost–benefit analysis of aerocapture at all atmosphere-bearing destinations. The study showed an increase of the delivered mass to Venus by 79% using aerocapture compared with propulsive option for a target circular orbit of 300 km altitude and 43% for an elliptical orbit of 300×8500 km. Fujita and Yamada [12] considered a Venus mission with an orbiter and an atmospheric balloon, in which aerocapture was used for the orbiter. The study showed that drag alternation using foldout decelerons is a viable control technique to perform small satellite (SmallSat) aerocapture on Venus.

In 2016, the NASA Jet Propulsion Laboratory (JPL) performed an A-Team study [6] funded by the NASA Planetary Science Division to determine the status of aerocapture technologies and assess their readiness for a mission. The study identified that no new technology developments are needed for aerocapture on Venus; however, investments in aerothermal analysis and TPS materials could enhance the mission. The study concluded that an aerocapture technology demonstration mission is not required to reduce risk prior to mission implementation.

In 2018, the Venus Exploration Analysis Group completed the Venus Bridge study report [13], which assessed viable Venus science missions within a $200 million cost cap using rideshare opportunities. This could include a multi-element mission, such as landers and balloons, and a SmallSat providing communication relay in addition to other scientific investigations from orbit. Drag-modulated aerocapture is an attractive option for SmallSats to perform OI from rideshare or flyby missions. A NASA study has investigated the entry environments and mechanical design for SmallSat using a single-event drag-modulated aerocapture on Venus [14].

Aerocapture on Venus has been shown to be feasible using existing technology, and allows a significant increase in delivered mass compared with propulsive OI [1,10]. There are comprehensive numerical studies addressing aerocapture feasibility at the ice giants [15] and Titan [16]. However, a comprehensive feasibility analysis of Venus aerocapture, applicability of different control methods, and detailed mass-benefit analysis is lacking in the literature. The paper considers constraints of the allowable aerocapture entry corridor, deceleration loads, peak heat rates, and total heat load, and presents the aerocapture design space using a graphical approach. Aerocapture feasibility charts are presented for two vehicle control techniques: lift modulation and drag modulation. Previous studies assessing the delivered mass benefit of aerocapture on Venus have assumed a constant aerocapture mass fraction, the ratio of aerocapture system mass to total entry vehicle mass. The current study estimates the payload mass fraction by taking into account the structural mass, control systems, and TPS using data from state-of-the-art entry systems. The delivered mass fraction using aerocapture is compared with propulsive insertion with and without aerobraking.

II. Methodology

A. Atmospheric Flight Mechanics

The position of a vehicle flying in the vicinity of a planet in a planet-centered and planet-fixed coordinate system is specified by its radial distance from the center of the planet r, longitude θ, and latitude ϕ. The angle between the velocity vector $\boldsymbol{V}$ and the local horizontal plane is the flight-path angle γ. The heading angle ψ is the angle between the projection of the velocity vector $\boldsymbol{V}$ on the local horizontal plane and the local parallel of latitude [17]. Kinematic equations that govern the evolution of these variables are [17]

$$\dot{r} = V \sin\gamma \tag{1a}$$

$$\dot{\theta} = \frac{V \cos\gamma \cos\psi}{r \cos\phi} \tag{1b}$$

$$\dot{\phi} = \frac{V \cos\gamma \sin\psi}{r} \tag{1c}$$

The dynamic equations of motion that govern the motion of the vehicle, including the gravity, aerodynamic, Coriolis, and centrifugal forces are [17–19]

$$\dot{V} = -\frac{q}{\beta} + g_r \sin\gamma + g_\theta \cos\gamma \cos\psi + g_\phi \cos\gamma \sin\psi + \Omega^2 r \cos\phi(\sin\gamma \cos\phi - \cos\gamma \sin\phi \sin\psi) \tag{2a}$$

$$\dot{\gamma} = \frac{q(L/D)}{V\beta}\cos\sigma + \frac{1}{V}(g_r \cos\gamma - g_\theta \sin\gamma \cos\psi - g_\phi \sin\gamma \sin\psi) + \frac{V\cos\gamma}{r} + \frac{\Omega^2 r}{V}\cos\phi(\cos\gamma \cos\phi + \sin\gamma \sin\phi \sin\psi) + 2\Omega \cos\phi \cos\psi \tag{2b}$$

$$\dot{\psi} = \frac{q(L/D)}{V\beta}\frac{\sin\sigma}{\cos\gamma} + \frac{1}{V\cos\gamma}(-g_\theta \sin\psi + g_\phi \cos\psi) - \frac{V}{r}\cos\gamma \cos\psi \tan\phi - \frac{\Omega^2 r}{V\cos\gamma}\sin\phi \cos\phi \cos\psi + 2\Omega(\tan\gamma \cos\phi \sin\psi - \sin\phi) \tag{2c}$$

in which σ is the bank angle, $\beta = m/(C_D A)$ is the vehicle ballistic coefficient, m is the vehicle mass, A is the aerodynamic reference area of the vehicle, $q = (1/2)\rho V^2$ is the dynamic pressure, $\rho = \rho(r, \theta, \phi)$ is the atmospheric density, Ω is the planet rotation rate about its spin axis, and V is the planet-relative vehicle speed. L is the lift force and D is the drag force, defined as

$$L = \frac{1}{2}\rho V^2 A C_L, \qquad D = \frac{1}{2}\rho V^2 A C_D \tag{3}$$

assuming the atmosphere is rotating with the planet at the planet's rotation rate, and the planet-relative and atmosphere-relative speeds are the same. C_L is the vehicle lift coefficient and C_D is the drag coefficient; g_r, g_θ, and g_ϕ are the radial, longitudinal, and latitudinal components of the gravitational acceleration, respectively, defined as [18,19]

$$g_r = \frac{\partial U}{\partial r}, \qquad g_\theta = \frac{1}{r\cos\phi}\frac{\partial U}{\partial \theta}, \qquad g_\phi = \frac{1}{r}\frac{\partial U}{\partial \phi} \tag{4}$$

in which U is the gravitational potential and is, in general, a function of r, θ, and ϕ. A simple representation of U can be expressed in terms of the zonal harmonic coefficients to fourth-order expansion [20]:

$$\begin{aligned} U = \frac{\mu_p}{r}\Bigg[1 &+ J_2\left(\frac{r_p}{r}\right)^2\left(\frac{1}{2} - \frac{3}{2}\sin^2\phi\right) \\ &+ J_3\left(\frac{r_p}{r}\right)^3\left(\frac{3}{2}\sin\phi - \frac{5}{2}\sin^3\phi\right) \\ &+ J_4\left(\frac{r_p}{r}\right)^4\left(-\frac{3}{8} + \frac{15}{4}\sin^2\phi - \frac{35}{8}\sin^4\phi\right)\Bigg] \end{aligned} \tag{5}$$

in which μ_p is the gravitational parameter of the planet; r_p is the mean equatorial radius of the planet; and J_2, J_3, and J_4 are the zonal harmonic terms. Venus has a slow rotation rate Ω and very small J_2 value compared with other planets. For aerocapture on Venus, the duration of the atmospheric flight is typically only a few minutes, and the rotation terms and higher-order gravity terms can be neglected in Eq. (2) without any significant loss of accuracy. However, these terms are retained for the generality of formulation, and may be required for an analysis of aerocapture guidance algorithms or for higher-fidelity simulations. The values of standard gravitational parameter μ_p, planetary radius r_p, rotation rate Ω (in which the $-$ve sign indicates retrograde), and zonal harmonic terms for Venus used in the simulations are listed in Table 1 and compared with Earth [21].

Given the initial conditions for the state variables $r_e, \theta_e, \phi_e, V_e, \gamma_e$, and ψ_e, in which the subscript denotes conditions at the atmospheric entry interface, Eqs. (1) and (2) can be used to determine the vehicle state during the atmospheric phase of aerocapture maneuver. A nondimensional form of the equations developed by Leszczynski [19] is used to avoid an ill-conditioned system during the numerical integration.

B. Atmosphere Model

Propagation of Eq. (2) requires the atmospheric density profile of the planet. The Venus Global Reference Atmospheric Model (Venus-GRAM) [22,23], an engineering-level atmosphere model developed by NASA, is widely used for system design and performance analysis of flight trajectories in the Venus atmosphere. Venus-GRAM outputs temperature, pressure, wind-speed components, and chemical composition as a function of altitude, latitude, longitude, and local solar time. Venus-GRAM also provides dispersion for thermodynamic parameters, density, and winds. The atmosphere model implemented in Venus-GRAM is based on the Venus International Reference Atmosphere model, which incorporates data from the Pioneer Venus (PV) Orbiter and Multiprobe and the Venera entry probes [24]. The current work uses the mean density profile only as a function of altitude, which is sufficient for preliminary aerocapture feasibility and performance-benefit analysis.

C. Arrival Conditions and Postcapture Orbit

The hyperbolic excess speed or arrival V_∞ and the declination δ with respect to the equatorial plane of the target planet are two important parameters that characterize the arrival conditions for an interplanetary transfer. The arrival V_∞ determines the inertial entry velocity $V_{e,i}$ at the atmospheric interface radius r_e:

$$V_{e,i}^2 = V_\infty^2 + \frac{2\mu_p}{r_e} \tag{6}$$

Venus rotation is neglected and inertial entry speed is assumed to be equal to the planet-relative entry speed V_e at the atmospheric interface. However, the velocity due to the rotating atmosphere cannot be neglected for entry at fast-rotating planets, such as Saturn and Neptune, and must be accounted for when computing V_e.

The desired orbit size and inclination depend on the science requirements and engineering constraints. Most previous orbiter missions to Venus used a near-polar high inclination orbit to get good latitudinal and longitudinal coverage as the planet rotates underneath. This study considers two target orbits: a low circular orbit of 400 km and an elliptical orbit of $400 \times 60{,}000$ km. The low circular orbit is representative of the one used by a radar mapping mission [25], an orbiter to study the atmosphere above the cloud layers, or a sample return mission orbiter that requires low circular Venus orbit to minimize the mass of the Venus ascent vehicle [26]. The elliptical orbit is representative of the one used in several previous and proposed Venus orbiter missions [27,28], as well as a communication relay orbiter for an aerial platform or lander [29]. To minimize the ΔV requirement for propulsive OI, mission planners select a highly elliptical initial orbit, and then use aerobraking over several months to 1 or 2 years to lower the apoapsis and enter the desired science orbit. Aerocapture, in contrast, achieves the desired science orbit immediately upon arrival, allowing science operations to begin earlier. Some missions require low circular orbit for science investigations, and aerocapture is an enabling technology if the time penalty for aerobraking is prohibitive.

The arrival declination δ constrains the range of possible inclinations for the postcapture orbit with the arrival declination limiting the minimum inclination orbit. However, a high-inclination polar orbit is achievable from any arrival trajectory by appropriately selecting the aim point on the B-plane [30]. High-inclination orbits allow global coverage of the planet, and therefore, are preferred for Venus orbiter missions. B-plane targeting can also accommodate other mission requirements, such as delivering lander, balloon, or other elements to a specific latitude.

D. Aerocapture Vehicles

The aerocapture vehicle serves two purposes: provide adequate aerodynamic control authority to compensate for navigation, atmospheric, and vehicle aerodynamic uncertainties; and protect the payload from severe aerodynamic heating during the maneuver. The control authority allows the onboard guidance algorithm to guide the spacecraft from the entry interface to the desired atmospheric exit state for the target capture orbit. This study considers two aerodynamic control approaches: lift modulation and drag modulation, as shown in Fig. 1.

Lift modulation uses an aeroshell that provides lift from offsetting the center of gravity with respect to the symmetry axis. Lift modulation control techniques include bank-angle modulation, angle of attack, and sideslip angle control [31,32], or a combination of these techniques. The current study considers only bank-angle modulation, in which the lift vector is rotated around the velocity vector by

Table 1 Comparison of planetary parameters of Venus and Earth [21]

Planet	μ_p, m^3/s^2	r_p, km	Ω, rad/s	$J_2(\times 10^{-6})$	$J_3(\times 10^{-6})$	$J_4(\times 10^{-6})$
Venus	3.248×10^{14}	6051.8	-2.992×10^{-7}	4.458	−1.93	−2.38
Earth	3.986×10^{14}	6378.1	7.272×10^{-5}	1082.6	−2.53	−1.62

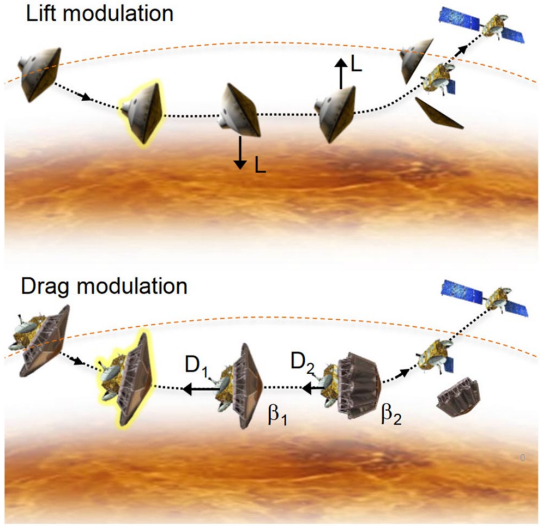

Fig. 1 Two aerodynamic control approaches for an aerocapture vehicle: lift modulation and drag modulation; dashed line indicates the atmospheric interface.

banking the vehicle, and the bank angle is the sole control variable. The aerodynamic control authority from a lift-modulated vehicle is determined by the hypersonic trim lift-to-drag ratio $(L/D)_{\text{trim}}$ at a specified (trim) angle of attack. The term $(L/D)\cos\sigma$ in Eq. (2) can be modulated between $+(L/D)_{\text{trim}}$ and $-(L/D)_{\text{trim}}$ by varying the bank angle σ from 0 to ± 180 deg. A bank angle of zero indicates full lift up, whereas 180 deg denotes full lift down. The guidance algorithm will continuously command the bank angle within this range during the atmospheric pass so that the vehicle achieves the desired exit conditions. Bank-angle modulation has been used on entry vehicles, such as Apollo and the Mars Science Laboratory (MSL) [33,34]. Aeroshells with $(L/D)_{\text{trim}}$ of up to 0.40 are low-L/D vehicles, 0.40–0.80 are mid-L/D aeroshells (such as the ellipsled), and $(L/D)_{\text{trim}} > 0.8$ are high-L/D vehicles [35]. Low-L/D aeroshells have flight heritage on planetary entry missions and are considered a mature technology, whereas mid- and high-L/D aeroshells need further development and testing [6]. Table 2 summarizes the achievable $(L/D)_{\text{trim}}$ for some past and proposed lifting aeroshells along with their notional technology readiness levels (TRLs). In addition to rigid aeroshells, lift modulation aerocapture can be performed using deployable entry systems, such as the lifting version of the Adaptive, Deployable Entry and Placement Technology (ADEPT) [36]. Deployable systems, such as ADEPT, offer two advantages: 1) small ballistic coefficient, which results in lower peak heat rate, and 2) open back shell, which relaxes the spacecraft packaging constraints. Deployable platforms are particularly attractive for SmallSats because the restrictive mass and volume on SmallSats prevent the use of a traditional rigid aeroshell for aerocapture, especially when launched as a secondary payload [37].

Drag modulation uses a nonlifting ($L/D = 0$) entry system with aerodynamic drag as the sole control variable by changing the vehicle reference drag area $C_D A$ during the atmospheric flight [38]. Two variants of this technique can be used: continuously variable and discrete-event drag modulation [39]. In continuously variable drag modulation, the drag area can be adjusted using deployable arms to expand or retract the drag skirt as commanded by the guidance algorithm. In discrete-event drag modulation, the vehicle can only have certain configurations (i.e., certain allowable ballistic coefficients), and the drag skirt(s) are jettisoned when the onboard guidance predicts that the vehicle will achieve the desired atmospheric exit conditions after drag skirt separation. The simplest variant is a single-event discrete drag modulation, in which the vehicle can only have two possible values of the ballistic coefficient β: a small-value β_1 with the drag skirt and a high-value β_2 after the drag skirt is jettisoned. The vehicle enters the atmosphere with the drag skirt allowing a small β during entry. The small ballistic coefficient lowers the aerodynamic heating rate as the vehicle decelerates at higher altitudes where the atmosphere is thinner [40]. The guidance algorithm predicts the target exit conditions if the drag skirt is jettisoned, and commands the drag skirt separation event when the predicted apoapsis is close to the target apoapsis [41]. The vehicle flies the remaining part of the trajectory with the high ballistic coefficient β_2. The control authority for the single-event discrete drag modulation is determined by the ballistic coefficient ratio before and after drag skirt separation β_2/β_1 [39], and is analogous to $(L/D)_{\text{trim}}$ for bank-angle modulation.

Table 2 L/D and TRL of some selected entry vehicles

Vehicle design	Planet	Mission	$(L/D)_{\text{trim}}$	TRL	References
70 deg sphere cone	Mars	Viking	0.18	High	[34]
70 deg sphere cone	Mars	MSL	0.24	High	[34]
Lifting ADEPT	Mars/Venus	— —	0.25	Mid	[35]
Sphere section	Earth	Apollo	0.36	High	[33]
Ellipsled	Neptune	— —	0.80	Low	[37]

E. Aerodynamic Heating and TPS

Aerocapture vehicles encounter aerothermodynamic heating during atmospheric pass at hypersonic speed, resulting in significant convective and radiative heat rates. TPS materials protect the payload from extreme heating, and the TPS material is chosen based on the peak stagnation-point aerothermal conditions. The complex physics involved in hypersonic, chemically reacting, high-temperature flows makes the accurate prediction of heating rates difficult [42]. Experimental testing often cannot fully recreate the severe conditions encountered during the flight, and ground test is often limited by the conditions achievable at the testing facility. Mission concept studies often use engineering correlations based on empirical relations or previous computational work to estimate the stagnation-point convective and radiative heating rates. The stagnation-point convective heating rate is estimated using the Sutton–Graves empirical relation [43]:

$$\dot{q}_c = K\left(\frac{\rho_\infty}{R_N}\right)^{0.5} V^3 \tag{7}$$

in which $\dot{q}_c$ is the stagnation-point convective heat flux in watts per square centimeter, $K = 1.896 \times 10^{-8}$ [44] for Venus entry; ρ_∞ is the freestream atmospheric density in kilograms per cubic meter; R_N is the vehicle nose radius in meters; and V is the freestream velocity in meters per second. The radiative heating is estimated using the following empirical relation [11,45]:

$$\dot{q}_r = \begin{cases} K_1 \rho_\infty^{1.2} V^{10.0} R_N^{0.49} & \text{if } V < 8000 \text{ m/s} \\ K_2 \rho_\infty^{1.2} V^{5.5} R_N^{0.49} & \text{if } 8000 \le V \le 10{,}000 \text{ m/s} \\ K_3 \rho_\infty^{1.2} V^{13.4} R_N^{0.49} & \text{if } 10{,}000 \le V \le 12{,}000 \text{ m/s} \end{cases} \tag{8}$$

in which $\dot{q}_r$ is the stagnation-point radiative heat flux in watts per square centimeter, $K_1 = 3.33 \times 10^{-34}$, $K_2 = 1.22 \times 10^{-16}$, and $K_3 = 3.07 \times 10^{-48}$. The correlation for $10{,}000 \le V \le 12{,}000$ m/s range is used for $V \ge 12{,}000$ m/s in this study, and may provide at best only an order-of-magnitude estimate of the radiative heating rates in this regime.

TPS materials can be divided into two categories: insulative/reusable and ablative. Insulative TPS, when exposed to atmospheric entry conditions, rejects heat by reradiation from the surface and internal storage. Insulative TPS is commonly used on reusable entry vehicles and can only withstand heat rates up to $\approx$100 W/cm^2. Examples of insulative TPS include the space shuttle tile and toughened unipiece fibrous reusable oxidation-resistant ceramic. Ablative TPS, when exposed to entry conditions, will pyrolyze and reject heat by blowing of pyrolysis products into the boundary layer [46]. Ablative TPS is commonly used on planetary entry probes and can withstand much higher heat rates up to $\approx$30,000 W/cm^2 [47].

Examples of ablative TPS include carbon phenolic (CP), which was used on the Galileo and PV entry probes, and phenolic-impregnated carbon ablator (PICA), which was used on stardust and MSL entry vehicles [46,48].

Despite the similar entry speeds on Earth and Venus, the thick CO_2-dominated Venusian atmosphere presents more demanding entry conditions than on Earth. PV entry probes used rigid aeroshells with a high ballistic coefficient and sustained heat rates of up to 5000 W/cm^2. CP was the only TPS material available that can withstand such heat rates. However, heritage CP is no longer available, as the raw material Avtex rayon is not being produced since 1986. To close the technology gap, NASA has been investing in a new ablative TPS material: Heatshield for Extreme Entry Environment Technology (HEEET). HEEET is a 3-D woven resin-infused material that has been tested for heat rates up to 8000 W/cm^2 and allows 40% mass savings compared with CP [49].

The peak stagnation-point heat rate, stagnation pressure, and stagnation-point heat load are important parameters for aerothermal design. The peak heat rate and stagnation pressure determine the type of TPS material. The TPS material must be qualified for heat rates and stagnation pressure conditions greater than or equal to the vehicle's entry requirement. The TPS thickness required at any given point on the heat shield is determined by the integrated heat load at that location [48]. A higher heat load implies a higher TPS mass fraction, and hence, a smaller payload mass fraction. The current study uses the stagnation-point heat load—the integral of the stagnation-point heat rate throughout the duration of the atmospheric flight to estimate the total TPS mass fraction. In certain situations, boundary-layer transition can cause afterbody heating rates to approach values at the stagnation point, and must be accounted for in TPS material selection and thickness. Estimating the TPS mass accurately during conceptual design is difficult, as the exact thicknesses and the types of TPS required are only available from a detailed flowfield and aerothermal analysis. Data from previous entry missions (involving only low-L/D blunt-body aeroshells) have been used to obtain a regression formula between the stagnation-point heat load Q and TPS mass fraction f_{TPS} for rigid low-L/D aeroshells as follows [50]:

$$f_{\mathrm{TPS}} = 0.091 Q^{0.51575} \tag{9}$$

in which Q has units of joule per square centimeter, and can be used to approximately estimate the TPS mass fraction for a blunt-body aeroshell. Table 3 summarizes some key aerothermodynamic parameters, TPS materials used, and f_{TPS} for several past missions [51–53].

Low ballistic coefficient systems (~10–50 kg/m^2) have been proposed as a potential solution to overcome the severe heating problems associated with conventional rigid high ballistic coefficient (~150–400 kg/m^2) entry systems on Venus [40]. Low ballistic coefficient vehicles may reduce the peak heating rate by a factor of 10. Mechanically deployed entry platforms (e.g., ADEPT) can be stowed in the launch fairing and deployed just before atmospheric entry to achieve ballistic coefficients as low as 10 kg/m^2. Woven carbon cloth has been proposed as the TPS material for such deployable entry systems and has been arcjet tested to 246 W/cm^2 at 9.6 kPa [54]. A drag modulation system that uses a rigid drag skirt and PICA TPS has been studied for aerocapture on Venus [14].

III. Aerocapture Feasibility

A. Theoretical Corridor Width

To successfully perform aerocapture, an entry vehicle must target the entry flight-path angle within the aerocapture corridor bounded by the minimum and maximum acceptable entry flight-path angles. The minimum entry flight-path angle $\gamma_{\min}$ or the undershoot boundary is the steepest at which the vehicle can enter and achieve the desired atmospheric exit conditions to achieve the target apoapsis. The maximum entry flight-path angle $\gamma_{\max}$ or the overshoot boundary is the shallowest allowable for the vehicle to achieve the desired orbit upon atmospheric exit. The difference between the two limiting entry flight-path angles is the theoretical corridor width (TCW), which is a measure of the control authority of the vehicle to compensate for uncertainties in navigation, atmospheric density, and vehicle aerodynamics:

$$\mathrm{TCW} = |\gamma_{\max} - \gamma_{\min}| \tag{10}$$

If the vehicle enters steeper than $\gamma_{\min}$, then the vehicle will bleed more speed than required. This will result in undershoot of the target apoapsis, and may cause the vehicle to burn up in the deep atmosphere or crash on the surface. If the vehicle enters shallower than $\gamma_{\max}$, the vehicle will not have decelerated enough upon atmospheric exit, resulting in overshoot of the target apoapsis or not getting captured at all. If the vehicle enters at any flight-path angle within the corridor bounds, then the aerocapture guidance algorithm will be able to successfully guide the vehicle to achieve the target orbit. When the vehicle is successfully captured, a small propulsive ΔV maneuver is performed at the apoapsis to raise the periapsis outside of the atmosphere. Additional propulsive maneuvers may be required to correct apoapsis errors and perform apo-twist maneuvers before the initial science orbit is established.

For bank-angle modulation, $\gamma_{\min}$ is the steepest flight-path angle at which the vehicle can enter while pointing the lift vector fully upward ($\sigma = 0$ deg) through the entire duration of the atmospheric flight. The shallowest allowable entry flight-path angle is $\gamma_{\max}$ in which lift vector points fully downward ($\sigma = 180$ deg) for the duration of the flight. TCW for bank-angle modulation primarily depends on the vehicle lift-to-drag ratio L/D and arrival V_∞, and to a lesser extent on the ballistic coefficient β. Figure 2 shows the two limiting flight-path angles for a lift modulation vehicle on Venus. In this study, entry flight-path angles are defined at an altitude of 150 km above Venus surface. The TCW varies slightly with target apoapsis altitude, but its effect is small (<10%) for capture orbits with apoapsis ranging from 400 to 1000 km. The results are reported for the target apoapsis altitude of 400 km, and targeting capture orbits with apoapsis altitude greater than 1000 km will result in lower TCW than reported in the current work.

For drag modulation, $\gamma_{\min}$ is the entry flight-path angle associated with the vehicle being successfully captured while flying with the highest ballistic coefficient possible (β_2). The limiting entry flight-

Table 3 Key aerothermodynamic parameters and TPS materials used in past entry missions

Entry vehicle	Planet/moon	β, kg/m^2	Peak heat rate, W/cm^2	Heat load, kJ/cm^2	TPS	f_{TPS}	Year (entry)
Apollo 17	Earth	396	392	33	Avcoat	0.13	1972
PV large probe	Venus	188	4,500	12.4	CP	0.10	1978
PV small "north"	Venus	190	7,200	11.7	CP	0.13	1978
PV small "day"	Venus	"	3,900	14.0	"	"	"
PV small "night"	Venus	"	2,300	12.5	"	"	"
Galileo	Jupiter	256	17,000	200	CP	0.50	1995
Mars Exploration Rover-B	Mars	88	44	3.6	SLA561-V	0.04	2004
Huygens	Titan	38	50	40	AQ60	0.30	2005
Stardust	Earth	60	1,200	36	PICA	0.22	2006
Hayabusa	Earth	114	1,500	32	CP	0.43	2007
MSL	Mars	146	197	5.47	PICA	0.12	2011

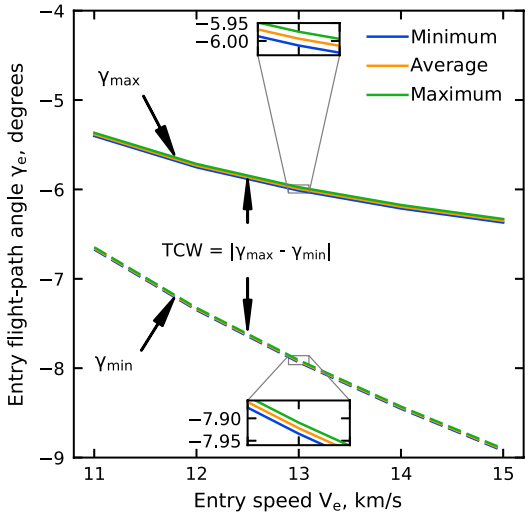

Fig. 2 Overshoot (solid) and undershoot (dashed) boundaries for a lift modulation aerocapture vehicle with $L/D = 0.24$, $\beta = 200$ kg/m^2 on Venus; inset shows the variation of corridor bounds for minimum, average, and maximum mean density profiles from Venus-GRAM.

path angle associated with the vehicle flying with the lowest ballistic coefficient β_1 for the entire atmospheric flight is $\gamma_{\max}$. The TCW for drag modulation aerocapture primarily depends on the ballistic coefficient ratio β_2/β_1 and arrival V_∞, and to a lesser extent on β_1 and the target apoapsis altitude.

The required corridor width (RCW) is a measure of the uncertainty in approach navigation, uncertainty in atmospheric density profile, and uncertainty in vehicle aerodynamic properties [37]. Lockwood et al. estimated that the uncertainty in entry flight-path angle ranges from ± 0.4 to ± 0.2 deg depending on whether the last update to the spacecraft inertial system is entry minus 48 or 5 h [10]. Considering the short light time of only a few minutes between Earth and Venus, it is reasonable to assume a navigation update can be made 5 h before entry, and the contribution of navigation uncertainty to RCW is 0.4 deg.

The contribution of the atmospheric and vehicle aerodynamic uncertainties to RCW has not been estimated for Venus in the literature. The simulations used in this study indicate that using the minimum and maximum mean density profiles from Venus-GRAM results in the corridor bounds changing by at most 0.05 deg for vehicle $L/D = 0.24$ entering at 13 km/s, as shown in Fig. 2. High-frequency density perturbations superposed on the mean variations not considered in this study will also contribute to the atmospheric uncertainty RCW component and will be investigated in future studies. An additional study is required to estimate the aerodynamic uncertainty component, and is outside the scope of the current work. Nominal aerodynamic uncertainties associated with a low-L/D vehicle performing aerocapture on Titan resulted in an RCW contribution of $\approx$1.0 deg [55], and could be a representative estimate for Venus aerocapture. The navigation, atmospheric, and aerodynamic uncertainties are root sum squared to compute the required RCW [37]. A larger TCW allows more safety margin over the computed RCW and enables the vehicle to compensate for larger uncertainties. Monte Carlo simulations can be used to estimate these uncertainties, but is outside the scope of the current work. For the vehicle to accomplish aerocapture

$$\text{TCW} \geq \text{RCW} + \epsilon \tag{11}$$

in which ϵ is a small additional margin over the computed RCW to allow for guidance not being able to successfully capture the entire corridor and other unaccounted uncertainties.

Failure to satisfy this criterion implies that the vehicle risks crashing into the planet, getting captured into a different orbit than desired, or not getting captured at all. Figure 3 shows the contours of the TCW, in degrees, for aerocapture on Venus with a lifting vehicle for two ballistic coefficients $\beta = 50$ and 500 kg/m^2 indicated by the solid and dashed lines respectively. L/D from 0 to 0.4 is chosen, 0.4 being an upper limit for heritage, low-L/D entry vehicles, as indicated in Table 2. A range of arrival V_∞ from 0 to 30 km/s is considered to represent a wide range of interplanetary trajectories. The upper limit of 30 km/s is chosen based on the Venus gravity assist flyby V_∞ for the Cassini–Huygens spacecraft en route to Saturn. For rigid aeroshells, $\beta = 50$ kg/m^2 is an estimated lower limit of the ballistic coefficient possible, and $\beta = 500$ kg/m^2 is used as an upper bound to illustrate the effect of ballistic coefficient variation. The two extremes of β are chosen so as to represent the range of ballistic coefficients expected for a bank-angle modulation system.

Figure 3 shows that the TCW increases with both increasing L/D and arrival V_∞. Higher L/D implies that the vehicle has more aerodynamic control authority, and can achieve desired atmospheric exit conditions from a wider range of entry flight-path angles than a lower-L/D vehicle, which increases the TCW. A higher arrival V_∞ allows the vehicle to enter at steeper angles to bleed more energy to get captured than a lower V_∞. Therefore, a higher arrival V_∞ (or corresponding V_e) offers a higher TCW, as can be seen in Figs. 2 and 3. The filled circle in Fig. 3 indicates that a vehicle with $L/D = 0.2$ and $\beta = 50$ kg/m^2 arriving at $V_\infty = 7.5$ km/s will achieve TCW = 1.5 deg. For arrival at $V_\infty = 7.5$ km/s, to achieve a TCW of 1.5 deg, a minimum L/D of 0.20 is required. In other words, with a vehicle of $L/D = 0.20$, an arrival V_∞ of 7.5 km/s or greater is required to achieve a TCW of 1.5 deg.

Given an RCW, points on the specified TCW contour lines in Fig. 3 can be used to find pairs of L/D and V_∞, which represent the minimum L/D or V_∞ required for aerocapture to be feasible. Equation (11) can be graphically interpreted as a constraint on the aerocapture design space in terms of L/D and V_∞. For an RCW of 1.5 deg, the 1.5 deg contour bounds the feasible design space (i.e., L/D and V_∞ combination); pairs of L/D and V_∞ lie on or above the contour of TCW = 1.5 deg satisfy Eq. (11), and therefore, are feasible design points. Figure 3 shows that the effect of ballistic coefficient on TCW is small. For the same value of L/D and V_∞, the vehicle has a slightly higher TCW with a lower ballistic coefficient.

Figure 4 shows the TCW contours in degrees for a single-event drag modulation for two initial low ballistic coefficients, $\beta_1 = 5$ kg/m^2 and $\beta_1 = 50$ kg/m^2, and ballistic coefficient ratio β_2/β_1 from 1 to 100. Note that, if $\beta_2/\beta_1 = 1$, the vehicle has no control authority (i.e., TCW = 0). For deployable entry systems, $\beta_2/\beta_1 = 100$ is a representative upper limit that can be achieved, and $\beta_1 = 5$–50 kg/m^2 is the range of ballistic coefficients expected for a drag modulation system.

In Fig. 4, the TCW increases with increasing β_2/β_1 and arrival V_∞. Higher β_2/β_1 implies that the vehicle has more control authority and can achieve desired atmospheric exit conditions from a wider range of entry flight-path angles than a vehicle with a smaller β_2/β_1. The filled circle indicates a vehicle with $\beta_1 = 5$ kg/m^2, and $\beta_2/\beta_1 = 27$

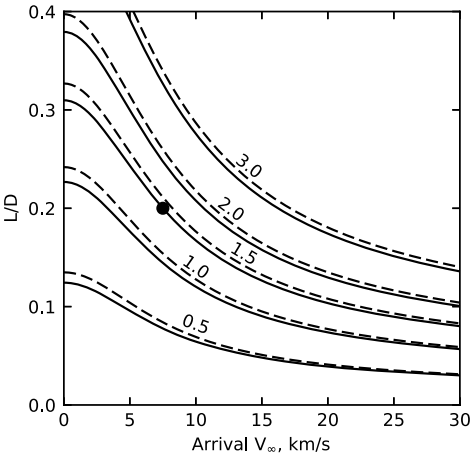

Fig. 3 TCW contours (deg) for lift modulation aerocapture with $\beta = 50$ kg/m^2 (solid lines) and $\beta = 500$ kg/m^2 (dashed lines).

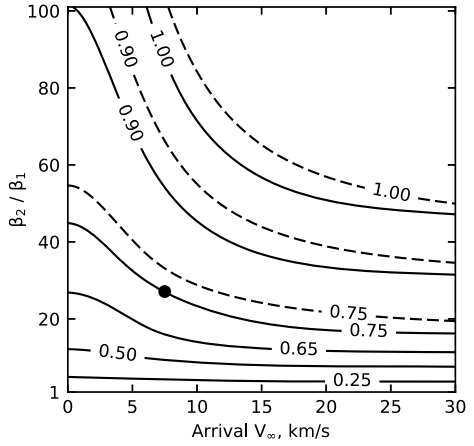

Fig. 4 TCW contours (deg) for drag modulation aerocapture with $\beta_1 = 5$ kg/m^2 (solid lines) and $\beta_1 = 50$ kg/m^2 (dashed lines).

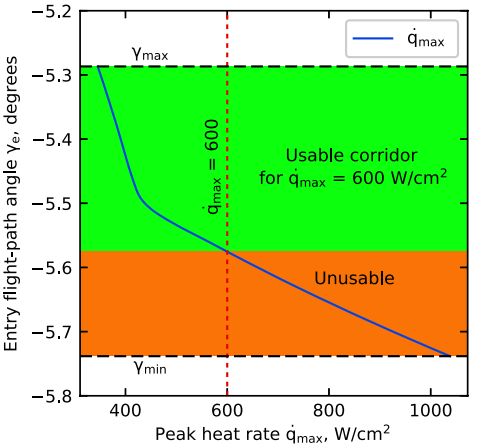

Fig. 5 Loss of corridor for single-event drag modulation aerocapture on Venus due to peak heat rate constraint; target apoapsis altitude = 400 km.

arriving at $V_\infty = 5$ km/s will achieve a TCW $= 0.75$ deg. Achieving a TCW of 0.75 deg at $V_\infty = 7.5$ km/s requires a minimum β_2/β_1 of 27.

Comparing Figs. 3 and 4, the TCW for drag modulation is smaller than that for lift modulation. Although a TCW of 1.5 deg is available with a heritage low-L/D MSL-like aeroshell ($L/D = 0.24$) for arrival V_∞ of 5 km/s or greater, a drag modulation system with $\beta_2/\beta_1 = 20$ offers only 0.65 deg for the same arrival V_∞. For deployable entry systems, $\beta_2/\beta_1 > 20$ may be difficult to implement due to the potential structural and packaging challenges of using a large drag area. The low TCW implies that drag modulation aerocapture will require navigation, atmospheric, and aerodynamic uncertainties to be lower than that required for lift modulation. Future studies will determine if entry flight-path angle errors from navigation and other uncertainties could be sufficiently reduced, so that a drag modulation system with practical β_2/β_1 offers sufficient TCW to satisfy Eq. (11). Monte Carlo simulations that incorporate all relevant uncertainties and guidance algorithms are required to fully analyze drag modulation aerocapture performance on Venus, and are recommended for future work.

It is noted that the entire width of the corridor computed in Fig. 4 is not generally available for a single-event drag modulation aerocapture. This is due to the fact that entry at the steep part of the corridor will require the large drag area to be jettisoned immediately after entry to hit the entry conditions for the target apoapsis altitude. This will result in the vehicle encountering peak heat rate with the high ballistic coefficient and compromises the ability of the vehicle to keep the heating rates low. To keep the peak heat rate within the material TPS capability, a part of the steep end of the entry flight-path angle corridor is unusable. For a vehicle with $\beta_1 = 31.4$ kg/m^2, $\beta_2/\beta_1 = 8.74$, and $R_N = 0.1$ m [56] entering at 11 km/s, if $\dot{q}_{\max}$ of 600 W/cm^2 is considered, the loss of corridor due to the peak heat rate constraint is shown in Fig. 5. If the allowable peak heat rate is lower than 600 W/cm^2, the usable corridor is further reduced. This implies the TCW computed in Fig. 4 represents an upper bound for the usable corridor, and the actual usable corridor is smaller. Delivery errors from approach navigation and other uncertainties should be low enough to fit within the usable aerocapture corridor. The fraction of the corridor rendered inaccessible due to the peak heat rate constraint depends on the specific vehicle design, nose radius, and entry conditions. Another important factor to be considered in single-event drag modulation aerocapture is the sensitivity of exit conditions to the drag skirt separation time. Retaining the drag skirt for just a few more seconds than the optimal separation time may result in the vehicle getting trapped in the atmosphere. Future studies will further investigate the aforementioned issues for a practical drag modulation system on Venus.

B. Peak Deceleration

The vehicle decelerates rapidly during the aerocapture maneuver with the trajectory changing from hyperbolic to elliptic in only a few minutes. The peak deceleration load G (measured in Earth g) to be sustained during the maneuver is an important design parameter. The aeroshell structure, orbiter payload, and onboard instruments are designed to withstand a maximum deceleration load $G_{\max}$, and this limit must not be exceeded during the aerocapture maneuver:

$$G \leq G_{\max} \tag{12}$$

For lift modulation aerocapture, the peak g load is the highest at the steep limit of the corridor, which results in the vehicle flying lift up during the entire trajectory. The g load for the steepest entry flight-path angle is the worst case, and therefore, denoted as peak g load and is used as a conservative estimate. Figure 6 shows the contours of the peak deceleration load for lift modulation aerocapture for this worst-case scenario as a function of L/D and arrival V_∞. The peak g load encountered increases with increasing L/D and arrival V_∞. The circle indicates that a vehicle with $L/D = 0.27$ with arrival $V_\infty = 5$ km/s will encounter a worst-case deceleration of $20g$. Note that this deceleration rate is only the quasi-steady-state component of the inertial loads. Turbulent buffeting not accounted for in the current analysis can significantly add to and increase the sensed deceleration. Scientific instruments are usually the most sensitive and must be designed to withstand the g loads during aerocapture. The small difference between the solid and dashed lines shows that the ballistic coefficient has a small effect on the peak deceleration. If $G_{\max} = 30g$, the $30g$ contour line bounds the feasible design space. Combinations of L/D and V_∞ that lie to the left of the contour line are feasible design points, whereas those to the right are infeasible. Guidance algorithms can

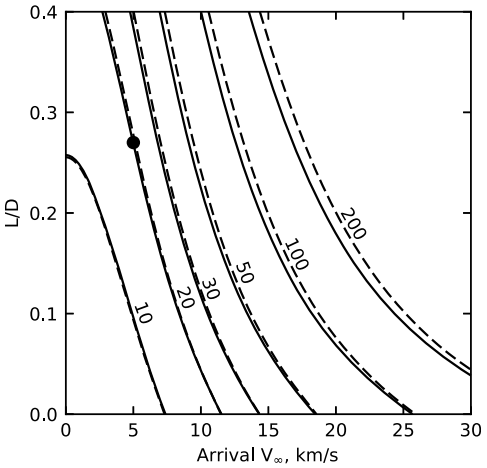

Fig. 6 Contours of peak deceleration (Earth g) for lift modulation aerocapture with $\beta = 50$ kg/m^2 (solid lines) and $\beta = 500$ kg/m^2 (dashed lines) corresponding to full lift-up undershoot trajectories.

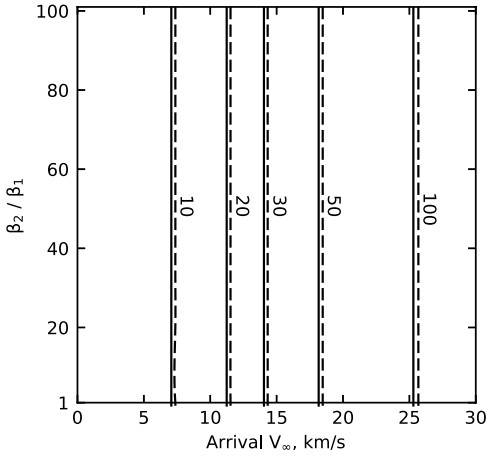

Fig. 7 Contours of peak deceleration (Earth g) for drag modulation aerocapture with $\beta_1 = 5$ kg/m^2 (solid lines) and $\beta_1 = 50$ kg/m^2 (dashed lines).

limit the peak g load to a lower value than the worst-case scenario in the current study while still providing sufficient corridor if the L/D is sufficiently high [11].

For drag modulation aerocapture, the peak g load is the highest for the shallowest entry flight-path angle, which results in the vehicle flying with the smallest ballistic coefficient β_1 (largest drag area) during the entire trajectory. Hence, the peak g load for the flight with β_1 is a conservative estimate of the actual value encountered in flight. Figure 7 shows the contours of the peak deceleration load for drag modulation aerocapture as a function of β_2/β_1 and arrival V_∞. Figure 7 uses β_2/β_1 on the vertical axis for consistency with other figures, although the worst-case g load (as defined for the purpose of this study) is independent of the β_2/β_1 ratio and depends only on the arrival V_∞ and β_1. The peak g load increases with increasing arrival V_∞, and the effect of β_1 is small.

C. Peak Heat Rate and Total Heat Load

Figure 8 shows the contours of stagnation-point peak heat rate for lift modulation aerocapture as a function of L/D and arrival V_∞ for $\beta = 50$ and 500 kg/m^2. The results are reported for a vehicle with an effective nose radius $R_N = 1$ m, which is representative of heritage blunt-body aeroshells. A smaller nose radius will increase the convective heating and decrease the radiative heating, as indicated by Eqs. (7) and (8). The worst-case peak heat rate occurs at the steepest entry flight-path angle, where the vehicle flies lift up ($\sigma = 0$ deg) during the entire trajectory. The peak heat rate contours in Fig. 8 correspond to the worst-case scenario. The peak heat rate is a strong function of the arrival V_∞, which in turn affects the entry speed V_e through Eq. (6) and the heating rates through Eqs. (7) and (8).

TPS materials are qualified to withstand a maximum heat rate $\dot{q}_{\max}$ along with maximum stagnation pressure and shear load. This study only considers the maximum heat rate limitation for the TPS material expressed as

$$\dot{q} \leq \dot{q}_{\max} \tag{13}$$

Currently, HEEET is the only available TPS material that can be used for lift modulation aerocapture on Venus. Other TPS materials, such as PICA (used on MSL), are inadequate to handle the peak heat rate of Venus entry, and hence, HEEET is an enabling technology for aerocapture on Venus. If $\dot{q}_{\max}$ of 5000 W/cm^2 is considered, then only the region to the left of the 5000 W/cm^2 contour line is feasible. This constrains the maximum arrival V_∞, and hence, imposes a constraint on the usable interplanetary trajectories.

The peak heat rate (shown in Fig. 8) has a strong correlation with ballistic coefficient, as seen from the large difference in contours corresponding to $\beta = 50$ kg/m^2 (solid lines) and $\beta = 500$ kg/m^2 (dashed lines). A vehicle with a higher ballistic coefficient does not slow down as much as one with a lower ballistic coefficient before reaching the lower altitude, higher density atmosphere, resulting in the higher β vehicle encountering a higher peak heating rate. The peak heat rate contours for the higher $\beta = 500$ kg/m^2 is to the left of those for $\beta = 50$ kg/m^2, indicating that, for a higher ballistic coefficient, the same peak heat rate occurs at a lower V_∞ than the lower β.

Figure 9 shows the contours of stagnation-point peak heat rate for drag modulation aerocapture as a function of β_2/β_1 and arrival V_∞ for $\beta_1 = 5$ and 50 kg/m^2. The results are reported for a vehicle with a deployed base diameter of 2 m and nose radius $R_N = 0.5$ m, assuming a scaled version of the nano-ADEPT concept [57]. A deployable entry system cannot use ablative TPS, such as HEEET, but instead uses foldable materials, such as carbon cloth, which can only accommodate significantly lower peak heat rates ≈400 W/cm^2. To keep the heat rates within the material limit, the large drag area (corresponding to β_1) must be retained until the vehicle passes through peak heating. The worst-case peak heat rate in Fig. 9 is reported for the steepest entry flight-path angle and the vehicle flies with the large drag area. The large difference between the solid and dashed lines indicates that ballistic coefficient strongly affects the peak heat rate, and a smaller ballistic coefficient is desired to keep the heating rates low.

Figure 10 shows the contours of stagnation-point total heat load Q for lift modulation aerocapture as a function of L/D and arrival V_∞ for $\beta = 50$ and 500 kg/m^2. The worst-case total heat load occurs for the shallowest entry flight-path angle, in which the vehicle flies lift down ($\sigma = 180$ deg) during the entire trajectory. Even though the shallow limit entry results in a lower peak heat rate than the steep limit

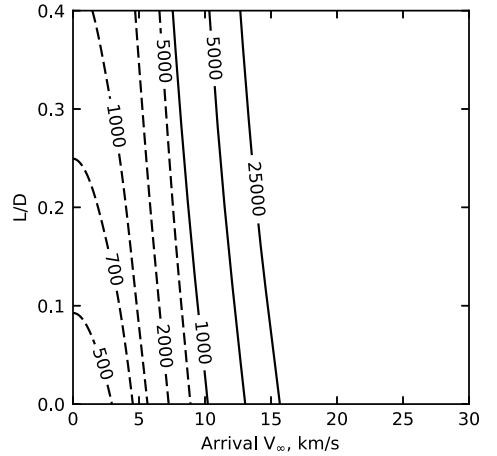

Fig. 8 Contours of peak heat rate (W/cm^2) for lift modulation aerocapture with $\beta = 50$ kg/m^2 (solid lines) and $\beta = 500$ kg/m^2 (dashed lines) corresponding to full lift up undershoot trajectories.

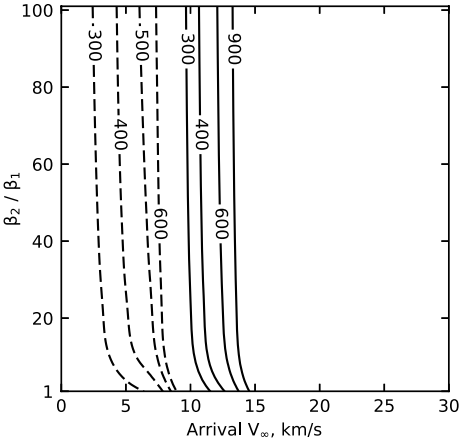

Fig. 9 Contours of peak heat rate (W/cm^2) for drag modulation aerocapture with $\beta_1 = 5$ kg/m^2 (solid lines) and $\beta_1 = 50$ kg/m^2 (dashed lines).

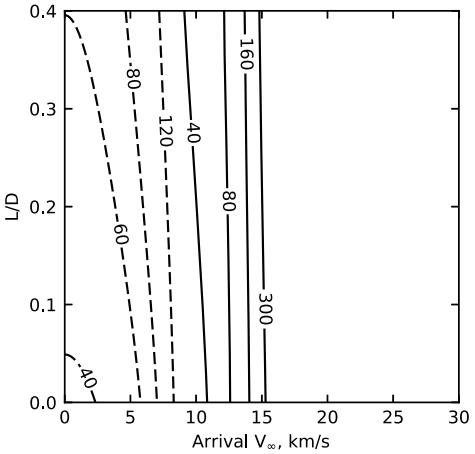

Fig. 10 Contours of total heat load (kJ/cm^2) for lift modulation aerocapture with $\beta = 50$ kg/m^2 (solid lines) and $\beta = 500$ kg/m^2 (dashed lines) corresponding to full lift-down overshoot trajectories.

entry, the shallow trajectory stays in the atmosphere for much longer, and hence, results in the larger total heat load than the steep limit trajectory. The heat load contours in Fig. 10 correspond to the worst-case shallowest entry scenario. The total heat load is a strong function of the arrival V_∞ and a weaker function of the L/D for the higher ballistic coefficient. The total heat load can be correlated to the vehicle TPS mass fraction using Eq. (9). To keep the TPS mass fraction at a reasonable level, a maximum allowable heat load Q_{max} can be specified, and the heat load constraint on aerocapture can be expressed as

$$Q \leq Q_{max} \tag{14}$$

Given a Q_{max}, the contour line in Fig. 10 corresponding to Q_{max} defines the feasible design space. This constraint limits the maximum acceptable V_∞ beyond which aerocapture is infeasible due to the excessive total heat load. As with the peak heat rate, the ballistic coefficient strongly affects the total heat load shown by the large difference between the solid and dashed lines. The larger ballistic coefficient results in more heating, whereas the smaller ballistic coefficient allows a larger arrival V_∞ for the same total heat load.

Figure 11 shows the contours of stagnation-point total heat load Q for drag modulation aerocapture as a function of β_2/β_1 and arrival V_∞ for $\beta = 5$ and 50 kg/m^2. The worst-case total heat load in Fig. 11

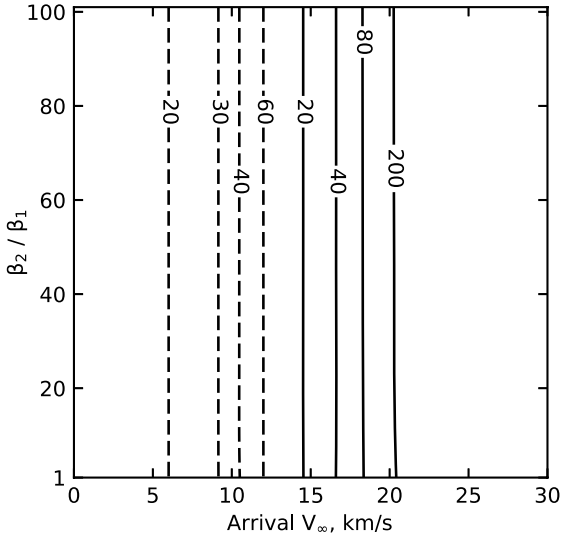

Fig. 11 Contours of total heat load (kJ/cm^2) drag modulation aerocapture with $\beta_1 = 5$ kg/m^2 (solid lines) and $\beta_1 = 50$ kg/m^2 (dashed lines).

corresponds to the steepest entry flight-path case, and the vehicle flies with the large drag area. The heat load depends only on β_1, as the vehicle is forced to keep its lowest ballistic coefficient β_1 through the peak aerodynamic heating to keep the peak heat rate within the material capability.

D. Aerocapture Feasibility Chart

The constraints can be combined into a single chart to visualize the feasible aerocapture design space spanning interplanetary arrival V_∞ and vehicle performance determined by $(L/D)_{trim}$ or β_2/β_1. Figure 12 shows the constraint lines corresponding to RCW = [1.0, 1.5] deg, $G_{max} = [30,50]g$, $\dot{q}_{max} = [7000, 40{,}000]$ W/cm^2, and $Q_{max} = [50,100]$ kJ/cm^2 for lift modulation aerocapture with $\beta = 50$ kg/m^2. The green shaded region indicates the feasible design space for RCW = 1.5 deg, $G_{max} = 30g$, $\dot{q}_{max} = 7000$ W/cm^2, and $Q_{max} = 50$ kJ/cm^2. The bottom right corner of the green region indicates that the lowest feasible vehicle L/D is 0.19 for an interplanetary trajectory with $V_\infty = 8.3$ km/s.

If the TCW requirement is lowered to 1.0 deg, then the yellow region becomes feasible in addition to the green region, and the vehicle L/D requirement can be lowered to 0.12 for $V_\infty = 9.8$ km/s. The lowest L/D occurs at the high end of arrival V_∞, as described in Sec. III.A. For a vehicle with a smaller arrival $V_\infty = 5$ km/s, which is a nominal value for Earth–Venus chemical trajectories, the required L/D is 0.18. Relaxing the peak deceleration constraint to $50g$, in addition to the TCW constraint being relaxed to 1.0 deg, results in the cyan and magenta regions also becoming feasible. This allows the L/D requirement to be lowered further, and also allows a higher arrival V_∞.

Figure 13 shows the corresponding feasible design space for lift modulation aerocapture with $\beta = 500$ kg/m^2. The high ballistic coefficient results in higher heat rates and heat loads compared with $\beta = 50$ kg/m^2. For a maximum allowable heat load of 50 kJ/cm^2, there is no feasible design space as the TCW constraint cannot be satisfied. To obtain a feasible region, the heat load constraint is required to be relaxed to 100 kJ/cm^2. The minimum required L/D, as indicated by the bottom right corner from the green (TCW = 1.5 deg) and yellow (TCW = 1.0 deg) regions, are 0.22 and 0.16, respectively, for the highest feasible V_∞.

Figures 14 and 15 show the constraints from TCW, g load, peak heat rate, and total heat load in a single plot for lift modulation aerocapture with $\beta = 50$ and 500 kg/m^2. A mission designer can choose the values of acceptable TCW, g load, peak heat rate, and total heat load to evaluate the aerocapture feasibility on Venus. Given an interplanetary trajectory, its arrival V_∞ can be used to calculate the minimum required L/D. Alternatively, given a vehicle L/D, the chart provides the range of feasible arrival V_∞. The constraints on the boundary of the feasible region indicate the limiting or driving constraints on aerocapture. From Fig. 12, it is apparent that, for the

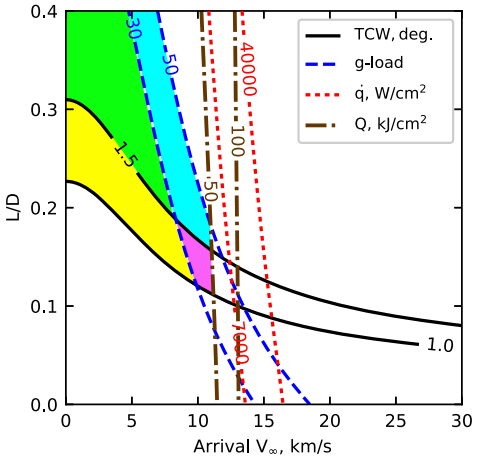

Fig. 12 Feasible design space for lift modulation aerocapture with $\beta = 50$ kg/m^2.

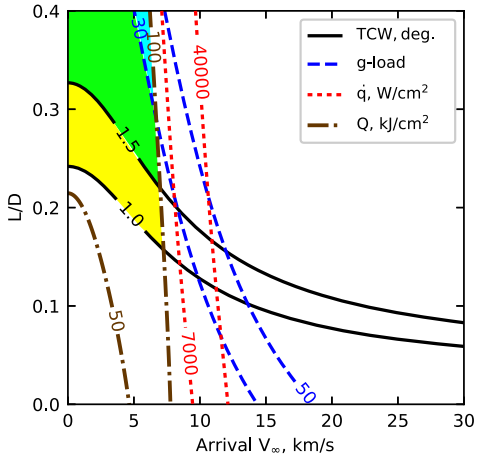

Fig. 13 Feasible design space for lift modulation aerocapture with $\beta = 500$ kg/m^2.

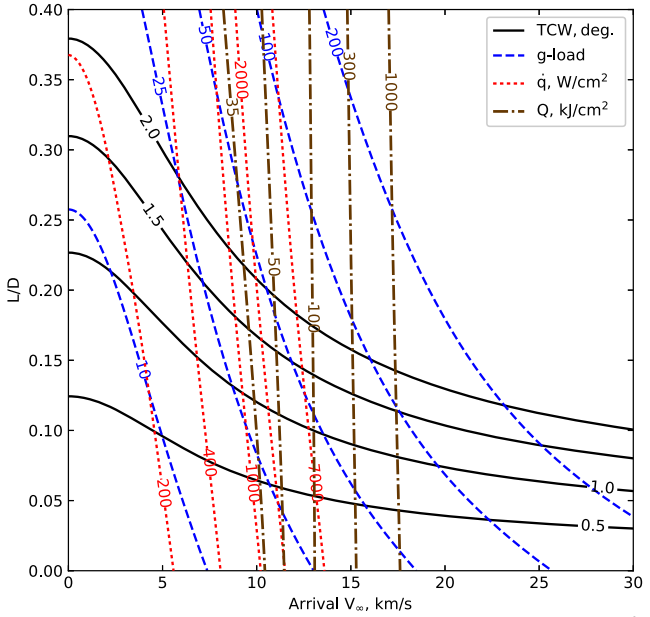

Fig. 14 Lift modulation aerocapture feasibility chart for $\beta = 50$ kg/m^2.

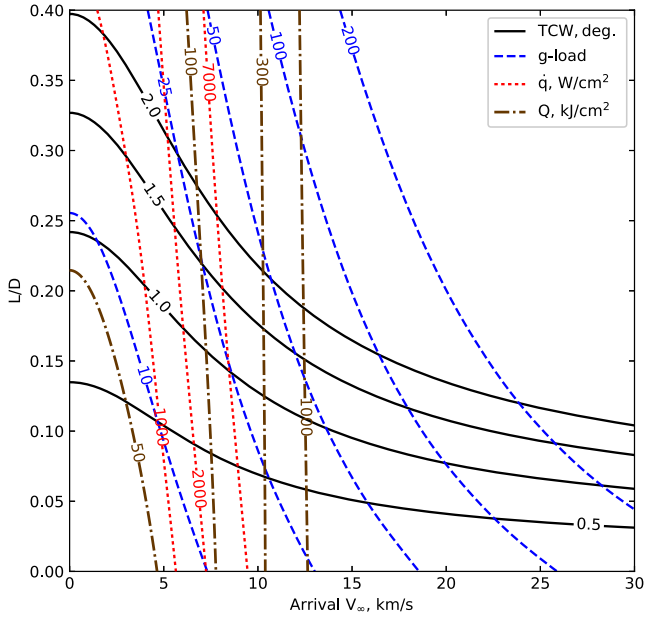

Fig. 15 Lift modulation aerocapture feasibility chart for $\beta = 500$ kg/m^2.

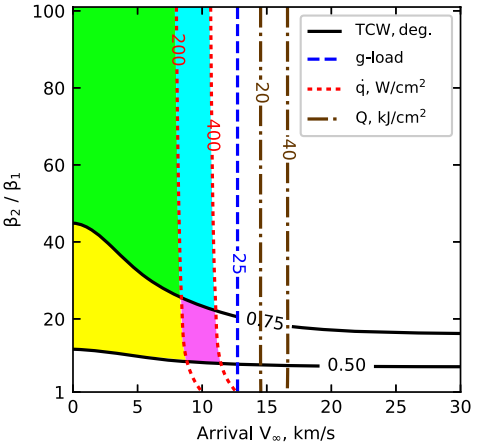

Fig. 16 Feasible design space for drag modulation aerocapture with $\beta_1 = 5$ kg/m^2.

particular constraint values considered, TCW and peak g load are the limiting factors.

The aerocapture feasibility charts show that the TCW constraint imposes a lower limit on the acceptable arrival V_∞, whereas the g load and heating constraints impose an upper limit on arrival V_∞. The charts show the coupling between the interplanetary trajectory and aerocapture vehicle performance, through the dependence on arrival V_∞. A high arrival V_∞ can lower the vehicle L/D requirement if it does not violate the heating or g-load constraints.

For drag modulation aerocapture, it is desired to minimize the β_2/β_1 required, as high β_2/β_1 ratios present significant engineering challenges associated with very large deployable entry systems. Figure 16 shows the constraint lines corresponding to RCW $= [0.50, 0.75]$ deg, $G_{\max} = 25g$, $\dot{q}_{\max} = [200, 400]$ W/cm^2, and $Q_{\max} = [20, 40]$ kJ/cm^2 for drag modulation aerocapture with $\beta_1 = 5$ kg/m^2. The green shaded region indicates the feasible design space for RCW $= 0.75$ deg, $G_{\max} = 25g$, $\dot{q}_{\max} = 200$ W/cm^2, and $Q_{\max} = 20$ kJ/cm^2. The bottom right corner of the green region indicates that the lowest feasible β_2/β_1 is 25 for a vehicle arriving at $V_\infty = 8.4$ km/s.

If the TCW requirement is lowered to 0.5 deg, then the yellow region becomes feasible in addition to the green patch, and the β_2/β_1 requirement can be lowered to 8.9 for a vehicle arriving at $V_\infty = 8.9$ km/s. For a vehicle with a smaller arrival $V_\infty = 5$ km/s, the required β_2/β_1 is 10.3. Relaxing the peak heat rate constraint to 400 W/cm^2, in addition to the TCW constraint being relaxed to 0.50 deg, results in the cyan and magenta regions also becoming feasible.

Figure 17 shows the corresponding feasible design space for drag modulation aerocapture with $\beta_1 = 50$ kg/m^2. The high ballistic coefficient results in higher heat rates and heat loads compared with $\beta_1 = 5$ kg/m^2. For a maximum allowable peak heat rate of 200 W/cm^2, there is no feasible design space as the TCW constraint cannot be satisfied. The heat rate constraint is required to be relaxed to 400 W/cm^2 to obtain a feasible region, and is the dominant constraint limiting the highest arrival V_∞. The minimum required β_2/β_1, as indicated by the bottom right corner from the green (TCW $= 1.5$ deg) and yellow (TCW $= 1.0$ deg) regions, are 41 and 11, respectively, for the highest feasible V_∞. Figures 18 and 19 show the constraints from TCW, g load, peak heat rate, and total heat load in a single plot for drag modulation aerocapture with $\beta_1 = 5$ and 50 kg/m^2.

IV. Mass-Benefit Analysis

A. Interplanetary Trajectory

Chemical interplanetary trajectories from Earth to Venus launching between 2018 and 2026 were generated using the STOUR software developed at JPL and upgraded at Purdue University for automated design of gravity assist trajectories [58,59]. STOUR is a low-fidelity broad search trajectory tool that allows multiple body

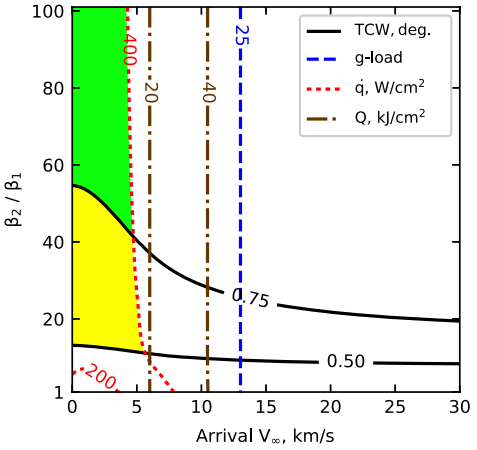

Fig. 17 Feasible design space for drag modulation aerocapture with $\beta_1 = 50$ kg/m^2.

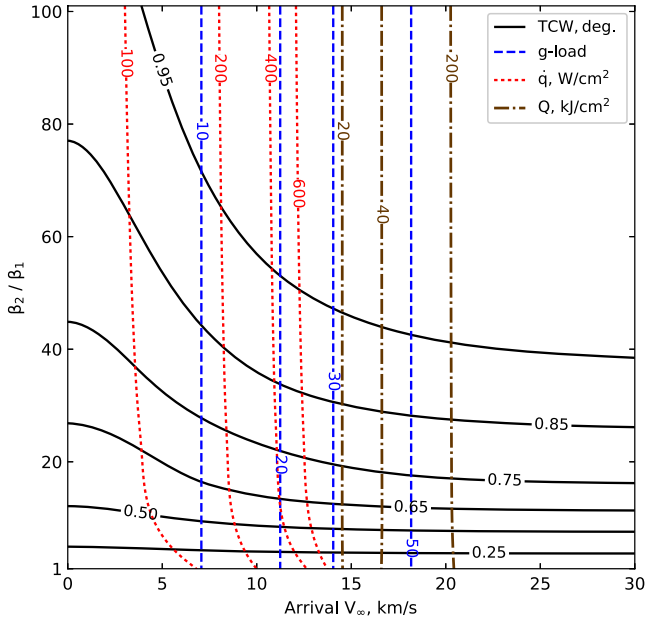

Fig. 18 Drag modulation aerocapture feasibility chart for $\beta_1 = 5$ kg/m^2.

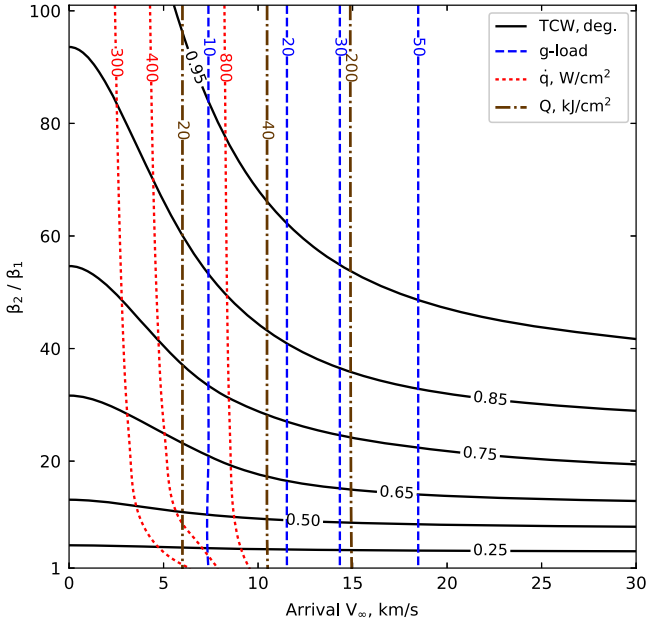

Fig. 19 Drag modulation aerocapture feasibility chart for $\beta_1 = 50$ kg/m^2.

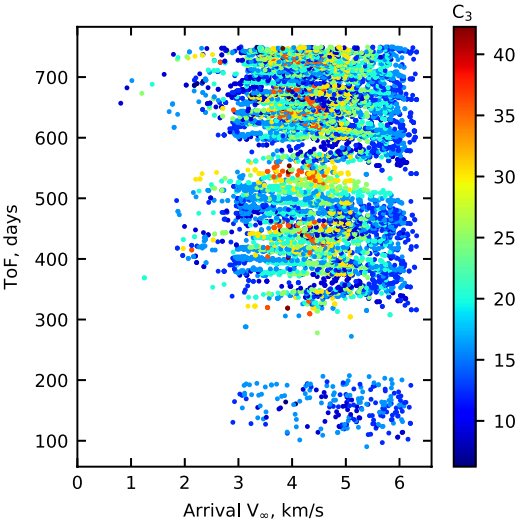

Fig. 20 Arrival V_∞, TOF, and launch C_3 for Earth–Venus interplanetary trajectories launching between 2018 and 2026.

gravity assist sequences along with user-specified ΔV constraint, and has been used in mission concept studies [60,61]. Launch dates spanning a period of 8 years are chosen, as the Earth–Venus orbital configuration approximately repeats every 8 Earth years and the trajectories are representative of the wide range of arrival conditions [62,63]. The search includes results for ballistic transfer from Earth to Venus, and with up to one deep-space maneuver (DSM) and one Venus flyby. Figure 20 summarizes key parameters, such as time of flight (TOF, days), arrival V_∞, and launch C_3 for the Earth–Venus trajectories used in the study.

B. Entry-System Payload Mass Fraction

In addition to TPS materials, the entry vehicle includes aeroshell structure, guidance systems, ballast masses, and other systems that are not useful payload. In the analysis, all systems (excluding the TPS materials) essential for aerocapture maneuver, but not usable payload, are lumped into a single parameter called entry-support-system mass M_{ESS}. Therefore, the total aerocapture vehicle entry mass can be broken down as

$$M_{\text{total}} = M_{\text{ESS}} + M_{\text{TPS}} + M_P \tag{15}$$

in which M_{TPS} is the TPS mass, and M_P is the useful payload mass (i.e., delivered mass to orbit). The usable payload mass fraction for the entry system $f_{P,\text{entry}}$ is computed as

$$f_{P,\text{entry}} = 1 - f_{\text{ESS}} - f_{\text{TPS}} \tag{16}$$

in which $f_{P,\text{entry}} = M_P/M_{\text{total}}$, entry-support-system mass fraction $f_{\text{ESS}} = M_{\text{ESS}}/M_{\text{total}}$, and TPS mass fraction $f_{\text{TPS}} = M_{\text{TPS}}/M_{\text{total}}$. The values of these mass fractions for aerocapture vehicle on Venus can only be computed accurately from a detailed vehicle design, which is outside the scope of the current study. There is a lack of architectural-level models of aerocapture systems for early mission concept studies in contrast to propulsive insertion, in which fairly accurate sizing relations are available [64]. To enable a preliminary comparison of aerocapture with propulsive insertion, available data for the existing entry vehicles are used to estimate the payload mass fraction for Venus entry. Table 4 lists the values of f_{ESS} and f_{TPS} for MSL and ADEPT Venus Intrepid Tessera Lander (ADEPT-VITaL) [65]. MSL is representative of low-L/D lifting aeroshell, which could be used for Venus aerocapture with HEEET TPS replacing the original PICA heat shield. ADEPT-VITaL is a Venus entry mission concept that could be adapted for drag modulation aerocapture. The original MSL vehicle TPS is designed to accommodate a heat load of $\approx$5 kJ/cm^2, whereas $\approx$35 kJ/cm^2 is expected for aerocapture on Venus for a vehicle with $L/D = 0.24$ entering the atmosphere at $V_e = 12$ km/s. To account for the higher heat load for Venus entry

Table 4 Mass fractions for past entry missions/concepts and estimated payload mass fraction on Venus

Entry vehicle	Planet	f_{ESS}	f_{TPS}	$f_{TPS,Venusentry}$	$f_{P,Venusentry}$	Details
MSL	Mars	0.23	0.12	0.19	0.58	Appendix A
ADEPT-VITaL	Venus	0.40	0.10	0.10	0.50	Appendix B

compared with Mars entry, $f_{\text{TPS,Venus entry}}$ is revised to 0.19 based on Eq. (9). Assuming f_{ESS} is equal to the original vehicle, the usable payload mass fraction for Venus entry $f_{P,\text{Venus entry}}$ is

$$f_{P,\text{Venus entry}} = 1 - f_{ESS} - f_{\text{TPS,Venus entry}} \tag{17}$$

Density differences in TPS materials and structural changes which may be required to adapt the entry vehicle into an aerocapture vehicle are not accounted for in $f_{P,\text{Venus entry}}$. Hence, the $f_{P,\text{Venus entry}}$ value must be regarded as a nominal estimate in the absence of a detailed Venus aerocapture vehicle design, and future studies will investigate its validity.

C. Mass-Benefit Analysis

The primary advantage of using aerocapture on Venus is the potential mass saving compared with propulsive OI. An analysis of the mass benefit of aerocapture using lift modulation and drag modulation systems has not been investigated comprehensively in the literature, which can be attributed to the difficulty in estimating the aerocapture delivered mass fraction without a detailed vehicle design, and the fact that previous studies often relied on a single interplanetary trajectory to compare aerocapture and propulsive options. The current analysis uses mass numbers of the state-of-the-art entry systems to estimate the aerocapture payload mass fraction, and uses a comprehensive set of interplanetary trajectories and different capture orbits to enable comparison of aerocapture with the propulsive option. This paper considers three Venus mission architectures to evaluate the potential mass benefit of aerocapture compared with propulsive capture with and without aerobraking: a dedicated mission to Venus; a SmallSat riding along with a mission flying to or by Venus; and a SmallSat that rides along with a lunar mission, and then transfers to Venus.

1. *Dedicated Mission to Venus*

This mission architecture requires a dedicated launch vehicle placing the spacecraft on an Earth–Venus trajectory. The OI ΔV_{OI} (for propulsive insertion) is then computed based on the arrival V_∞ and the target capture orbit assuming an impulsive burn at the periapsis:

$$\Delta V_{OI} = \sqrt{V_\infty^2 + \frac{2\mu_p}{r_{pe}}} - V_{pe} \tag{18}$$

in which r_{pe} is the periapsis of the target capture orbit, and V_{pe} is the orbital speed at periapsis of the target capture orbit. The useful payload mass fraction for purely propulsive insertion $f_{P,prop}$ for dedicated missions defined as the fraction of Earth escape mass that can be delivered into Venus orbit is

$$f_{P,prop} = \exp\left[-\frac{\Delta V_{DSM}}{I_{sp} g_0}\right]\left(1 - 1.12\left(1 - \exp\left[-\frac{\Delta V_{OI}}{I_{sp} g_0}\right]\right)\right) \tag{19}$$

in which ΔV_{DSM} is the DSM ΔV, I_{sp} is the engine specific impulse in seconds, $g_0 = 9.80665$ m/s^2 is the standard gravitational acceleration on Earth, and 1.12 represents a 12% tankage factor to account for the mass of the propulsion system. The aforementioned tankage factor is applicable for current large, space-storable, bipropellant propulsion systems. The useful payload mass fraction for aerocapture OI $f_{P,ac}$ for dedicated missions is

$$f_{P,ac} = \exp\left[-\frac{\Delta V_{DSM}}{I_{sp} g_0}\right] f_{P,\text{Venus entry}} - f_{\text{Cruise stage}} \tag{20}$$

in which $f_{P,\text{Venus entry}}$ is the Venus entry-system useful payload mass fraction calculated in Sec. IV.B; $f_{\text{Cruise stage}}$ accounts for an MSL-like cruise stage mass fraction (≈0.1) jettisoned prior to aerocapture.

2. *SmallSat Rideshare on Venus Mission*

The rideshare option involves a SmallSat riding along as a secondary payload with another mission flying to or by Venus, and is released a few weeks before the carrier spacecraft arrives on Venus. The SmallSat is assumed to be allotted a maximum allowable ride-along mass of 180 kg and enough volume to carry an ADEPT-like deployable entry system on the carrier spacecraft. Because of the mass and volume constraints for secondary payloads, it is not feasible for lifting a rigid aeroshell like MSL to be used in the rideshare architecture. SmallSats typically do not have bi-prop engines used by large orbiters, but have mono-prop engines with a lower $I_{sp} = 230$ s. The useful payload mass fraction $f_{P,prop}$ for rideshare missions is defined as the fraction of allowable ride-along mass that can be delivered into Venus orbit using propulsive insertion. Equation (19) is used to compute $f_{P,prop}$ with $\Delta V_{DSM} = 0$, assuming any ΔV_{DSM} is performed by the carrier spacecraft. The fraction of allowable ridealong mass that can be delivered into Venus orbit using aerocapture denoted by $f_{P,ac}$, is equal to $f_{P,\text{Venus entry}}$ described in Sec. IV.B.

For a carrier spacecraft flying to Venus (i.e. The carrier spacecraft performs orbit insertion or probe entry at Venus.), V_∞ from the interplanetary trajectory data set is used. For a spacecraft that is using Venus for a gravity assist and is flying by Venus on its way elsewhere in the inner solar system or the asteroid belt, a nominal $V_\infty = 10$ km/s is used. Missions flying by Venus and on to Jupiter and the outer solar system typically have $V_\infty \gg 10$ km/s. Such high flyby V_∞ trajectories cannot be used to get a secondary payload into orbit using a propulsive technique because of the quasi- exponential increase of the propellant mass required for ΔV_{OI} and the heat rate limitation on TPS for aerocapture.

3. *SmallSat Rideshare on a Lunar Mission*

This option involves a SmallSat riding along as a secondary payload with a lunar mission, and subsequently uses Earth/moon flybys and chemical or electric propulsion to transfer to Venus. The useful payload mass fraction $f_{P,prop}$ for lunar rideshare missions is defined as the fraction of mass delivered to the lunar vicinity that can be inserted into Venus orbit. The propulsive payload mass fraction $f_{P,prop}$ for this architecture is computed using Eq. (19) with ΔV_{DSM} replaced by ΔV_{escape}, in which ΔV_{escape} is the propulsive ΔV required to escape Earth's sphere of influence from the lunar vicinity. Mission design options presented in a recent Venus SmallSat study indicate that using ΔV_{escape} of ≈270 m/s along with Earth and moon flybys can place the spacecraft on a transfer trajectory to Venus [66]. The trajectory had an arrival $V_\infty \approx 3.8$ km/s and is used to compute ΔV_{OI}. The useful payload mass that can be inserted into orbit using aerocapture $f_{P,ac}$ is computed using Eq. (20) with ΔV_{DSM} replaced by ΔV_{escape}, and $f_{\text{Cruise stage}} = 0$. A deployable SmallSat entry system with an open back shell is assumed to not require a separate cruise stage.

D. Mass Benefit of Aerocapture

Figure 21 shows the payload mass fraction for propulsive OI $f_{P,prop}$ for ballistic chemical trajectories to Venus launching between 2018 and 2027, capturing into a 400 × 60,000 km orbit. A standard bi-prop engine with I_{sp} of 323 s is assumed. The results are from a broad trajectory search (same as in Fig. 20) and indicate the most favorable launch opportunities that occur from 2023 to 2025. During the most favorable launch opportunities from 2023–2025

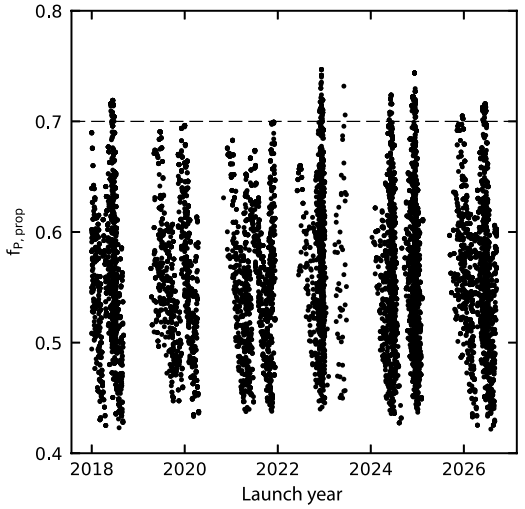

Fig. 21 Propulsive insertion payload mass fraction $f_{P,\text{prop}}$ to $400 \times 60{,}000$ km Venus orbit. During the most favorable launch opportunities from 2023–2025, $f_{P,\text{prop}} \geq 0.70$ can be achieved.

$f_{P,\text{prop}} \geq 0.70$ can be achieved. The corresponding nominal $f_{P,\text{prop}}$ to a 400×400 km orbit is 0.25.

Figure 22 compares the payload mass fraction that can be delivered to a 400 km circular Venus orbit with different OI techniques for the mission architectures described in Sec. IV.C. For aerobraking, the spacecraft first propulsively captures into an elliptical $400 \times 60{,}000$ km orbit, and over the course of several months gradually lowers the orbit to 400×400 km using multiple upper atmospheric passes. The gradual apoapsis reduction using aerobraking is assumed to consume a negligible propellant, and hence, the entire delivered mass to the initial capture orbit is available in the low circular orbit.

Figure 22 shows that propulsive capture followed by aerobraking delivers the highest mass fraction to orbit for all mission architectures considered except for the rideshare with a mission flying by Venus for a gravity assist. The elliptical initial capture orbit minimizes the OI ΔV_{OI} and results in Eq. (19) delivering a higher mass fraction compared with aerocapture, which is limited by the entry-system useful mass fraction. Entry-system payload mass fraction is in the range of 0.5–0.6 for state-of-the-art entry systems considered in this study, and this limits the maximum aerocapture payload mass fraction. While the entry-system payload mass fraction is relatively insensitive to ΔV for the range of arrival $V_\infty < 6$ km/s, propulsive insertion mass with the lower ΔV offers a significant improvement. Although propulsive insertion to the highly elliptical orbit is able to fully exploit this benefit, aerocapture is hampered by the entry support systems and the significant TPS mass required for the demanding Venus entry. The current study found that the entry-system payload mass fraction needs to be improved to at least 0.7 for aerocapture to offer mass benefit compared with propulsive insertion into an elliptical orbit around Venus. For the case of a SmallSat riding along as a secondary payload on a mission flying by Venus for a gravity assist, the high $V_\infty \approx 10$ km/s results in prohibitively high ΔV for a propulsive technique to deliver a reasonable payload mass even to a highly elliptical orbit. Aerocapture, however, can accommodate the higher heat rate (up to the TPS limit) and heat loads arising from this higher speed entry using a higher TPS mass fraction, and still achieve a reasonable payload mass fraction.

Figure 22 shows that purely propulsive insertion results in the lowest payload mass fraction for all mission architectures, as the high ΔV_{OI} requires a prohibitively high propellant mass to achieve the 400 km circular orbit. Although low circular orbits are preferred for radar mapping [67], data relay satellite for balloon missions [68], and sample return missions, such orbits cannot be achieved using propulsive insertion alone. Propulsive capture to a highly elliptical orbit followed by aerobraking to the low circular orbit is the most mass-efficient option if the time of several months is acceptable. If low circular Venus orbit is critical for the mission science and time penalty is not acceptable as in the case of a SmallSat whose life may be only a few months, aerocapture allows the low circular orbit to be achieved immediately upon arrival.

Aerocapture offers an increase in delivered mass to a low circular Venus orbit compared with purely propulsive insertion. For dedicated missions to Venus, aerocapture using an MSL-derived aeroshell delivers 90% more mass into a 400 km orbit compared with propulsive insertion using a bi-prop engine. For a SmallSat rideshare with a mission flying to Venus, aerocapture using an ADEPT-derived entry system delivers 250% more mass to a 400 km circular orbit than propulsive insertion using a mono-prop engine. For a SmallSat as a secondary payload on a mission flying by Venus at high V_∞ for a gravity assist, aerocapture is an enabling option to perform OI. For a SmallSat rideshare with a lunar mission, aerocapture delivers 140% more mass compared with propulsive insertion.

V. Conclusions

The current study indicates that aerocapture is a feasible OI technique on Venus and allows an increased delivered mass to a low Venus orbit compared with propulsive insertion. Both lift modulation and drag modulation have been studied with respect to their TCW, peak deceleration, peak heat rate, and total heat load. Lift modulation aerocapture on Venus is feasible with existing MSL-like low-L/D aeroshells and HEEET TPS. Drag modulation aerocapture is an attractive option for SmallSats as secondary payloads given its small

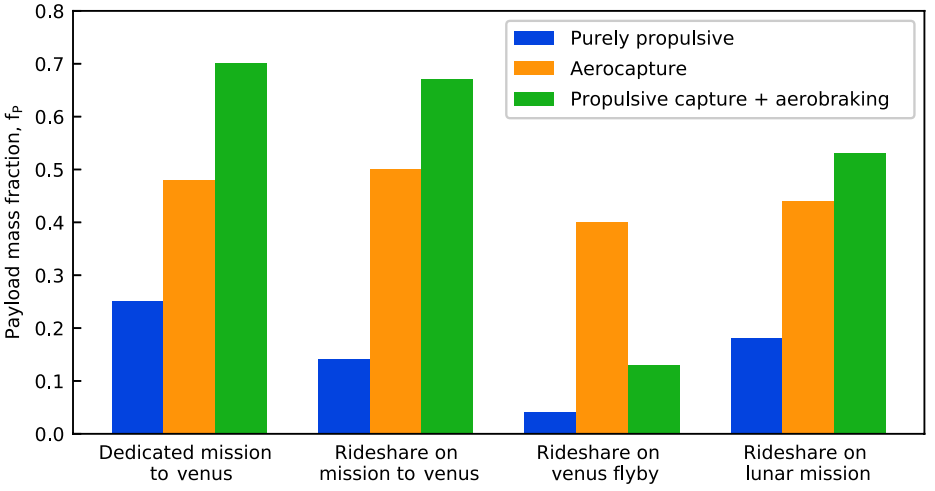

Fig. 22 Comparison of payload mass fraction delivered to a 400 km circular Venus orbit with different OI techniques for various mission architectures.

mass and volume footprint on a carrier spacecraft. A future study to further investigate the constraints arising from a small corridor width and heating rate is recommended for drag modulation on Venus. The constraints have been combined into a single plot to visualize the Venus aerocapture feasible design space for both lift- and drag modulation techniques. The aerocapture feasibility charts allow a mission designer to rapidly assess aerocapture feasibility for selected constraint values, and determine the vehicle L/D or β_2/β_1 required along with the range of acceptable arrival V_∞. A detailed analysis of Earth–Venus trajectories and a useful mass fraction delivered by entry systems is used to assess the mass benefit of aerocapture on Venus. Aerocapture offers significant mass benefit to future radar mapping missions, sample return missions, and other missions for which a low circular Venus orbit is highly desirable. Propulsive capture to a highly elliptical orbit followed by aerobraking to a low circular orbit is the most attractive option for OI on Venus, if the time penalty of several months to a few years for aerobraking is acceptable. If a low Venus orbit is desired immediately upon arrival, aerocapture allows for 90–250% increase in delivered mass to a 400 km circular orbit compared with propulsive insertion depending on the mission architecture.

Appendix A: Mars Science Laboratory Mass Breakdown[§]

Table A1 Mass breakdown for Mars Science Laboratory entry system

System	Mass, kg	Type
Back shell	450	ESS
Front shell + heat shield	385	TPS
Rover	899	P
Ballast (2×75 kg)	150	ESS
Ballast (6×25 kg)	150	ESS
Skycrane (dry)	829	P
Skycrane propellant	387	P
Parachute	50	P
Total	3300	

ESS = entry support system; TPS = thermal protection system; P = Payload.

Appendix B: Adaptive Deployable Entry and Placement Technology Mass Breakdown

Table B1 Mass breakdown for Adaptive Deployable Entry and Placement Technology entry system

System	Mass, kg	Type
Structure	392	ESS
Mechanisms	205	ESS
Avionics and power	17	ESS
Back shell	30	ESS
TPS (carbon cloth)	92	TPS
TPS (rigid nose)	71	TPS
Payload	813	P
Total	1620	

ESS = entry support system; TPS = thermal protection system; P = Payload.

Acknowledgments

The authors acknowledge the efforts of Alec Mudek at Purdue University for generating the Earth–Venus trajectory data using STOUR. The authors would like to thank James A. Cutts and Thomas W. Thompson at the NASA Jet Propulsion Laboratory for their initiative, support, and feedback in this study. Portions of this work were presented at the NASA Venus Exploration Analysis Group (VEXAG) meetings held in 2017 and 2018 at the Johns Hopkins University Applied Physics Laboratory. VEXAG student travel support for Athul Pradeepkumar Girija and Ye Lu to attend these meetings is gratefully acknowledged. Feedback provided by scientists, engineers, and program managers at the VEXAG meetings helped in the completion of this study, and is gratefully acknowledged.

[§]http://planet4589.org/space/jsr/back/news.664.txt [retrieved 17 December 2019].

References

[1] Hall, J. L., Noca, M. A., and Bailey, R. W., "Cost-Benefit Analysis of the Aerocapture Mission Set," *Journal of Spacecraft and Rockets*, Vol. 42, No. 2, 2005, pp. 309–320. https://doi.org/10.2514/1.4118

[2] Carpenter, R., "Aeroassist Flight Experiment," Texas Space Grant Consortium, Tech. Rept. ASE 396, Univ. of Texas, Austin, Nov. 1992, http://www.tsgc.utexas.edu/archive/PDF/AeroassistFlightExp.pdf [retrieved 17 Dec. 2019].

[3] Powell, R., "Numerical Roll Reversal Predictor Corrector Aerocapture and Precision Landing Guidance Algorithms for the Mars Surveyor Program 2001 Missions," *23rd Atmospheric Flight Mechanics Conference*, AIAA Paper 1998-4574, Aug. 1998. https://doi.org/10.2514/6.1998-4574

[4] Cazaux, C., Naderi, F., Whetsel, C., Beaty, D., Gershman, B., Kornfeld, R., Mitcheltree, B., and Sackheim, B., "The NASA/CNES Mars Sample Return—A Status Report," *Acta Astronautica*, Vol. 54, No. 8, 2004, pp. 601–617. https://doi.org/10.1016/j.actaastro.2003.07.001

[5] Keys, A., Hall, J., Oh, D., and Munk, M., "Overview of a Proposed Flight Validation of Aerocapture System Technology for Planetary Missions," *42nd AIAA/ASME/SAE/ASEE Joint Propulsion Conference and Exhibit*, AIAA Paper 2006-4518, July 2006. https://doi.org/10.2514/6.2006-4518

[6] Spilker, T. R., Adler, M., Arora, N., Beauchamp, P. M., Cutts, J. A., Munk, M. M., Powell, R. W., Braun, R. D., and Wercinski, P. F., "Qualitative Assessment of Aerocapture and Applications to Future Missions," *Journal of Spacecraft and Rockets*, Vol. 56, No. 2, 2018, pp. 1–10. https://doi.org/10.2514/1.A34056

[7] Repic, E. M., Boobar, M. G., and Chapel, F. G., "Aerobraking as a Potential Planetary Capture Mode," *Journal of Spacecraft and Rockets*, Vol. 5, No. 8, 1968, pp. 921–926. https://doi.org/10.2514/3.29389

[8] Menees, G. P., "Trajectory Analysis of Radiative Heating for Planetary Missions with Aerobraking of Spacecraft," *Journal of Spacecraft and Rockets*, Vol. 22, No. 1, 1985, pp. 37–45. https://doi.org/10.2514/3.25707

[9] Cruz, M., "The Aerocapture Vehicle Mission Design Concept," *Conference on Advanced Technology for Future Space Systems*, AIAA Paper 1979-893, May 1979. https://doi.org/10.2514/6.1979-893

[10] Lockwood, M. K., Starr, B. R., Paulson, J. W., Kontinos, D. A., Chen, Y. K., Laub, B., et al., "Systems Analysis for a Venus Aerocapture Mission," NASA TM-2006-214291, 2006, https://ntrs.nasa.gov/archive/nasa/casi.ntrs.nasa.gov/20060010899.pdf [retrieved 17 Dec. 2019].

[11] Craig, S., and Lyne, J. E., "Parametric Study of Aerocapture for Missions to Venus," *Journal of Spacecraft and Rockets*, Vol. 42, No. 6, 2005, pp. 1035–1038. https://doi.org/10.2514/1.2589

[12] Fujita, K., and Yamada, T., "Preliminary Study of Venus Exploration with Aerocapture System," *AIAA Atmospheric Flight Mechanics Conference and Exhibit*, AIAA Paper 2008-6392, Aug. 2008. https://doi.org/10.2514/6.2008-6392

[13] Grimm, R., Gilmore, M., Cutts, J., Hunter, G., Herrick, R., Izenberg, N., Jessup, K. L., Landau, D., Lillis, R., Oleson, S., et al., "Venus Bridge Summary Report," Tech. Rept., 2018, https://www.lpi.usra.edu/vexag/reports/Venus_Bridge_Summary_Report.pdf [retrieved 17 Dec. 2019].

[14] Nelessen, A., Austin, A., Ravich, J., Strauss, B., Venkatapathy, E., Beck, R., Wercinski, P., Wilder, M., Allen, G., Aftomis, M., et al., "Small Satellite Aerocapture for Increased Mass Delivered to Venus and Beyond," *15th International Planetary Probe Workshop*, Jet Propulsion Lab, Pasadena, CA, 2018, https://www.colorado.edu/event/ippw2018/sites/default/files/attached-files/smallprobes_1_nelessen_presid622_presslides_docid1143.pdf [retrieved 17 Dec. 2019].

[15] Saikia, S., Millane, J., Mudek, A., Arora, A., Witsberger, P., Shibata, E., Podesta, L., Lu, Y., Edelman, P., Longuski, J., et al., "Aerocapture Assessment at Uranus and Neptune for NASA's Ice Giant Studies,"

Purdue Univ., Tech. Rept. PU-AAC-2016-MC-0002, West Lafayette, IN, 2016.
[16] Lu, Y., and Saikia, S. J., "Feasibility Assessment of Aerocapture for Future Titan Orbiter Missions," *Journal of Spacecraft and Rockets*, Vol. 55, No. 5, 2018, pp. 1125–1135. https://doi.org/10.2514/1.A34121
[17] Vinh, N. X., Busemann, A., and Culp, R. D., *Hypersonic and Planetary Entry Flight Mechanics*, Univ. of Michigan Press, Ann Arbor, MI, 1980, pp. 26–28.
[18] Pontani, M., and Teofilatto, P., "Post-Aerocapture Orbit Selection and Maintenance for the Aerofast Mission to Mars," *Acta Astronautica*, Vol. 79, Oct.–Nov. 2012, pp. 168–178. https://doi.org/10.1016/j.actaastro.2012.04.020
[19] Leszczynski, Z. V., "Modeling, Simulation and Visualization of Aerocapture," Naval Postgraduate School, Tech. Rept., Monterey, CA, 1998, https://calhoun.nps.edu/handle/10945/32660 [retrieved 17 Dec. 2019].
[20] Vallado, D. A., *Fundamentals of Astrodynamics and Applications*, Vol. 12, Microcosm Press, El Segundo, CA, 2001, p. 147.
[21] de Pater, I., *Planetary Sciences*, 2nd ed., Cambridge Univ. Press, New York, 2010, p. 250.
[22] Justus, C., Duvall, A., and Keller, V., "Atmospheric Models for Aerocapture," *40th AIAA/ASME/SAE/ASEE Joint Propulsion Conference and Exhibit*, AIAA Paper 2004-3844, July 2004. https://doi.org/10.2514/6.2004-3844
[23] Duvall, A., Justus, C., and Keller, V., "Global Reference Atmospheric Model (GRAM) Series for Aeroassist Applications," *43rd AIAA Aerospace Sciences Meeting and Exhibit*, AIAA Paper 2005-1239, Jan. 2005. https://doi.org/10.2514/6.2005-1239
[24] Zasova, L., Moroz, V., Linkin, V., Khatuntsev, I., and Maiorov, B., "Structure of the Venusian Atmosphere from Surface up to 100 km," *Cosmic Research*, Vol. 44, No. 4, 2006, pp. 364–383. https://doi.org/10.1134/S0010952506040095
[25] Ghail, R., Wilson, C., Widemann, T., Bruzzone, L., Dumoulin, C., Helbert, J., et al., "EnVision: Understanding Why Our Most Earth-Like Neighbour is So Different," *ArXiv e-prints*, 2017, https://arxiv.org/abs/1703.09010 [retrieved 17 Dec. 2019].
[26] Cutts, J. A., Balint, T. S., Chassefiere, E., and Kolawa, E. A., "Technology Perspectives in the Future Exploration of Venus," *Geophysical Monograph Series*, Vol. 176, Jan. 2007, p. 207. https://doi.org/10.1029/176GM13
[27] Svedhem, H., Titov, D., Taylor, F., and Witasse, O., "Venus Express Mission," *Journal of Geophysical Research: Planets*, Vol. 114, No. E5, 2009. https://doi.org/10.1029/2008JE003290
[28] Anon., "Announcement of Opportunity (AO) to International Science Community for Space-Based Experiments to Study Venus," ISRO, Tech. Rept., Bangalore, India, 2018, https://www.isro.gov.in/sites/default/files/ao_venus.pdf [retrieved 17 Dec. 2019].
[29] Phipps, A., Woodroffe, A., Gibbon, D., Cropp, A., Joshi, M., Alcindor, P., Ghafoor, N., da Silva Curiel, A., Ward, J., Sweeting, M., et al., "Venus Orbiter and Entry Probe: An ESA Technology Reference Study," *8th ESA Workshop on Advanced Space Technologies for Robotics and Automation 'ASTRA 2004'*, ESA Publications Division, ESTEC, Noordwijk, Netherlands, Nov. 2004, http://robotics.estec.esa.int/ASTRA/Astra2004/Papers/astra2004_F-01.pdf [retrieved 17 Dec. 2019].
[30] Sergeyevsky, A. B., Snyder, G. C., and Cunniff, R. A., "Interplanetary Mission Design Handbook. Volume 1, Part 2: Earth to Mars Ballistic Mission Opportunities, 1990–2005," NASA Jet Propulsion Lab. Tech. Rept. JPL-PUBL-82-43-VOL-1-PT-2, Pasadena, CA, 1983, https://ntrs.nasa.gov/archive/nasa/casi.ntrs.nasa.gov/19840010158.pdf [retrieved 17 Dec. 2019].
[31] Jits, R. Y., and Walberg, G. D., "Blended Control, Predictor–Corrector Guidance Algorithm: An Enabling Technology for Mars Aerocapture," *Acta Astronautica*, Vol. 54, No. 6, 2004, pp. 385–398. https://doi.org/10.1016/S0094-5765(03)00159-0
[32] Davis, J., Dwyer Cianciolo, A., Powell, R., Shidner, J., and Garcia-Llama, E., "Guidance and Control Algorithms for the Mars Entry, Descent and Landing Systems Analysis," *AIAA/AAS Astrodynamics Specialist Conference*, AIAA Paper 2010-7972, Aug. 2010. https://doi.org/10.2514/6.2010-7972
[33] Hillje, E. R., "Entry Flight Aerodynamics from Apollo Mission AS-202," NASA TN D-4185, Oct. 1967, https://ntrs.nasa.gov/archive/nasa/casi.ntrs.nasa.gov/19670027745.pdf [retrieved 17 Dec. 2019].
[34] Way, D. W., Powell, R. W., Chen, A., Steltzner, A. D., San Martin, A. M., Burkhart, P. D., and Mendeck, G. F., "Mars Science Laboratory: Entry, Descent, and Landing System Performance," *2007 IEEE Aerospace Conference*, IEEE, New York, March 2007, pp. 1–19. https://doi.org/10.1109/AERO.2007.352821
[35] Venkatapathy, R., "Ballistic and Lifting Nano ADEPT Flight Testing for Mission Infusion Opportunities," *NASA Outer Planets Assessment Group (OPAG) Meeting*, Lunar and Planetary Inst., Houston, TX, Aug. 2016, https://www.lpi.usra.edu/opag/meetings/aug2016/posters/Venkatapathy.pdf [retrieved 17 Dec. 2019].
[36] Cassell, A., Smith, B., Wercinski, P., Ghassemieh, S., Hibbard, K., Nelessen, A., and Cutts, J., "ADEPT, A Mechanically Deployable Re-Entry Vehicle System, Enabling Interplanetary CubeSat and Small Satellite Missions," *32nd Annual AIAA/USU Conference on Small Satellites*, AIAA/Utah State Univ., Logan, UT, Aug. 2018, https://digitalcommons.usu.edu/smallsat/2018/all2018/265/ [retrieved 17 Dec. 2019].
[37] Lockwood, M. K., Edquist, K. T., Starr, B. R., Hollis, B. R., Hrinda, G. A., Bailey, R. W., Hall, J. L., Spilker, T. R., Noca, M. A., and O'Kongo, N., "Aerocapture Systems Analysis for a Neptune Mission," NASA TM-2006-214300, 2006, https://ntrs.nasa.gov/archive/nasa/casi.ntrs.nasa.gov/20060012088.pdf [retrieved 17 Dec. 2019].
[38] Putnam, Z. R., and Braun, R. D., "Analytical Assessment of Drag-Modulation Trajectory Control for Planetary Entry," *Journal of the Astronautical Sciences*, Vol. 65, No. 4, 2018, pp. 470–489. https://doi.org/10.1007/s40295-018-0134-z
[39] Putnam, Z. R., and Braun, R. D., "Drag-Modulation Flight-Control System Options for Planetary Aerocapture," *Journal of Spacecraft and Rockets*, Vol. 51, No. 1, 2014, pp. 139–150. https://doi.org/10.2514/1.A32589
[40] Dutta, S., Smith, B., Prabhu, D., and Venkatapathy, E., "Mission Sizing and Trade Studies for Low Ballistic Coefficient Entry Systems to Venus," *2012 IEEE Aerospace Conference*, IEEE, New York, 2012, pp. 1–14. https://doi.org/10.1109/AERO.2012.6187002
[41] Roelke, E., Werner, M., and Braun, R. D., "Single-Stage Drag Modulation GNC Performance for Venus Aerocapture Demonstration," *AIAA SciTech 2019 Forum*, AIAA Paper 2019-0016, Jan. 2019. https://doi.org/10.2514/6.2019-0016
[42] Gnoffo, P. A., Weilmuenster, K. J., Hamilton, H. H., Olynick, D. R., and Venkatapathy, E., "Computational Aerothermodynamic Design Issues for Hypersonic Vehicles," *Journal of Spacecraft and Rockets*, Vol. 36, No. 1, 1999, pp. 21–43. https://doi.org/10.2514/2.3430
[43] Sutton, K., and Graves, R. A., Jr., "A General Stagnation-Point Convective Heating Equation for Arbitrary Gas Mixtures," NASA TR-R-376, 1971, https://ntrs.nasa.gov/archive/nasa/casi.ntrs.nasa.gov/19720003329.pdf [retrieved 17 Dec. 2019].
[44] Samareh, J. A., "A Multidisciplinary Tool for Systems Analysis of Planetary Entry, Descent, and Landing (SAPE)," NASA TM-2009-215950, 2009, https://ntrs.nasa.gov/archive/nasa/casi.ntrs.nasa.gov/20090041828.pdf [retrieved 17 Dec. 2019].
[45] Page, W., and Woodward, H., "Radiative and Convective Heating During Venus Entry," *AIAA Journal*, Vol. 10, No. 10, 1972, pp. 1379–1381. https://doi.org/10.2514/3.6632
[46] Johnson, S. M., "Thermal Protection Materials and Systems: Past, Present, and Future," NASA Ames Research Center, TR ARC-E-DAA-TN9472, 2013, https://ntrs.nasa.gov/archive/nasa/casi.ntrs.nasa.gov/20130014035.pdf [retrieved 17 Dec. 2019].
[47] Laub, B., Wright, M. J., and Venkatapathy, E., "Thermal Protection System Design and the Relationship to Atmospheric Entry Environments," *6th International Planetary Probe Workshop*, IPPW, 2008, https://pub-lib.jpl.nasa.gov/docushare/dsweb/Get/Document-4950/Day1Laub.ppt.pdf [retrieved 17 Dec. 2019].
[48] Wright, M., "Aerothermodynamic and Thermal Protection System Aspects of Entry System Design Course," *Thermal and Fluids Analysis Workshop*, NASA Jet Propulsion Lab., Pasadena, CA, Aug. 2012, https://tfaws.nasa.gov/TFAWS12/Proceedings/Aerothermodynamics%20Course.pdf [retrieved 17 Dec. 2019].
[49] Venkatapathy, E., Ellerby, D., Wercinski, P., and Gage, P., "Venus Entry Challenges and Solutions for Aerial Platform Deployment," *Venus Aerial Platform Workshop #2*, Pasadena, CA, Dec. 2017, https://ntrs.nasa.gov/archive/nasa/casi.ntrs.nasa.gov/20180000811.pdf [retrieved 17 Dec. 2019].
[50] Laub, B., and Venkatapathy, E., "Thermal Protection System Technology and Facility Needs for Demanding Future Planetary Missions," *Proceedings of the International Workshop on Planetary Probe Atmospheric Entry and Descent Trajectory Analysis and Science*, Vol. 544, ESA Publ. Division, Noordwijk, The Netherlands, 2004, pp. 239–247, https://adsabs.harvard.edu/abs/2004ESASP.544..239L [retrieved 17 Dec. 2019].
[51] Orloff, R., and Garber, S., "Apollo by the Numbers: A Statistical Reference," NASA SP-2000-4029, 2000, https://ntrs.nasa.gov/archive/nasa/casi.ntrs.nasa.gov/20010008244.pdf [retrieved 17 Dec. 2019].

[52] Davies, C., and Arcadi, M., "Planetary Mission Entry Vehicles Quick Reference Guide. Version 3.0," NASA SP-2006-3401, 2006, https://ntrs.nasa.gov/archive/nasa/casi.ntrs.nasa.gov/20070022789.pdf [retrieved 17 Dec. 2019].

[53] Edquist, K. T., Hollis, B. R., Dyakonov, A. A., Laub, B., Wright, M. J., Rivellini, T. P., Slimko, E. M., and Willcockson, W. H., "Mars Science Laboratory Entry Capsule Aerothermodynamics and Thermal Protection System," *2007 IEEE Aerospace Conference*, IEEE, New York, March 2007, pp. 1–13. https://doi.org/10.1109/AERO.2007.352823

[54] Arnold, J. O., Chen, Y.-K., Prabhu, D. K., Bittner, M., and Venkatapathy, E., "Arcjet Testing of Woven Carbon Cloth for Use on Adaptive Deployable Entry Placement Technology," NASA Ames Research Center, TR ARC-E-DAA-TN6341, 2013, https://ntrs.nasa.gov/archive/nasa/casi.ntrs.nasa.gov/20130011056.pdf [retrieved 17 Dec. 2019].

[55] Lockwood, M. K., Queen, E. M., Way, D. W., Powell, R. W., Edquist, K., Starr, B. W., Hollis, B. R., Zoby, E. V., Hrinda, G. A., and Bailey, R. W., "Aerocapture Systems Analysis for a Titan Mission," NASA TM-2006-214273, 2006, https://ntrs.nasa.gov/archive/nasa/casi.ntrs.nasa.gov/20060007561.pdf [retrieved 17 Dec. 2019].

[56] Werner, M., Roelke, E., and Braun, R., "Dynamic Propagation of Discrete-Event Drag Modulation for Venus Aerocapture," *15th International Planetary Probe Workshop*, IPPW, 2018, https://www.colorado.edu/event/ippw2018/sites/default/files/attached-files/modsimvalid_9_werner_presid694_presslides_docid1218.pdf [retrieved 17 Dec. 2019].

[57] Smith, B., Cassell, A., Kruger, C., Venkatapathy, E., Kazemba, C., and Simonis, K., "Nano-ADEPT: An Entry System for Secondary Payloads," *2015 IEEE Aerospace Conference*, IEEE, New York, 2015, pp. 1–11. https://doi.org/10.1109/AERO.2015.7119095

[58] Rinderle, E. A., "Galileo Users Guide, Mission Design System, Satellite Tour Analysis and Design Subsystem," NASA Jet Propulsion Lab. TR JPL-D-263, Pasadena, CA, 1986.

[59] Longuski, J. M., and Williams, S. N., "Automated Design of Gravity-Assist Trajectories to Mars and the Outer Planets," *Celestial Mechanics and Dynamical Astronomy*, Vol. 52, No. 3, 1991, pp. 207–220. https://doi.org/10.1007/BF00048484

[60] Henning, G. A., Edelman, P. J., and Longuski, J. M., "Design and Optimization of Interplanetary Aerogravity-Assist Tours," *Journal of Spacecraft and Rockets*, Vol. 51, No. 6, 2014, pp. 1849–1856. https://doi.org/10.2514/1.A32881

[61] Mansell, J., Kolencherry, N., Hughes, K., Arora, A., Chye, H. S., Coleman, K., Elliott, J., Fulton, S., Hobar, N., Libben, B., et al., "Oceanus: A Multi-Spacecraft Flagship Mission Concept to Explore Saturn and Uranus," *Advances in Space Research*, Vol. 59, No. 9, 2017, pp. 2407–2433. https://doi.org/10.1016/j.asr.2017.02.012

[62] Chapman, D. M. F., "Recurrent Phenomena of Venus and the Venus/Earth Orbital Resonance," *Journal of the Royal Astronomical Society of Canada*, Vol. 80, Dec. 1986, pp. 336–343, http://adsabs.harvard.edu/abs/1986JRASC..80..336C [retrieved 17 Dec. 2019].

[63] Scafetta, N., "The Complex Planetary Synchronization Structure of the Solar System," arXiv preprint arXiv:1405.0193, 2014, https://arxiv.org/abs/1405.0193 [retrieved 17 Dec. 2019].

[64] Elliot, J., Reh, K., Hofstadter, M. D., and Simon, A., "Ice Giants Pre-Decadal Study Final Report," NASA TR JPL D-100520, 2017, https://www.lpi.usra.edu/icegiants/mission_study/ [retrieved 17 Dec. 2019].

[65] Smith, B., Venkatapathy, E., Wercinski, P., Yount, B., Prabhu, D., Gage, P., Glaze, L., and Baker, C., "Venus In Situ Explorer Mission Design Using a Mechanically Deployed Aerodynamic Decelerator," *2013 IEEE Aerospace Conference*, IEEE, New York, March 2013, pp. 1–18. https://doi.org/10.1109/AERO.2013.6497176

[66] Oleson, S., Izenberg, N., Gilmore, M., Jessup, K. L., Herrick, R., Balcerski, J., Landis, G., Hunter, G., Neudeck, P., Beheim, G., et al., "V-BOSS: Venus Bridge Orbiter and Surface System Preliminary Report," *15th NASA Venus Exploration Analysis Group Meeting*, VEXAG, Laurel, MD, 2017, https://www.lpi.usra.edu/vexag/meetings/archive/vexag_15/presentations/21-COMPASS-Venus-Bridge-Summary.pdf [retrieved 17 Dec. 2019].

[67] de Oliveira, M. R., Gil, P. J., and Ghail, R., "A Novel Orbiter Mission Concept for Venus with the EnVision Proposal," *Acta Astronautica*, Vol. 148, July 2018, pp. 260–267. https://doi.org/10.1016/j.actaastro.2018.05.012

[68] Grimm, R., "Venus Bridge: A Smallsat Program Through the Mid-2020s," *15th Venus Exploration and Analyis Group (VEXAG) Meeting*, VEXAG, Laurel, MD, 2018, https://www.lpi.usra.edu/vexag/meetings/archive/vexag_15/presentations/19-Grimm-Venus-Bridge-Focus-Group.pdf [retrieved 17 Dec. 2019].

K. T. Edquist
Associate Editor